Molecules with ALMA at Planet-forming Scales (MAPS) XII. Inferring the C/O and S/H ratios in protoplanetary disks with sulfur molecules

Le Gal, R.; Öberg, K.I.; Teague, R.; Loomis, R.A.; Law, C.J.; Walsh, C.; ... ; Zhang, K.

The Astrophysical Journal Supplement Series, 257:12 (20pp), 2021 November https://doi.org/10.3847/1538-4365/ac2583

Molecules with ALMA at Planet-forming Scales (MAPS). XII. Inferring the C/O and S/H Ratios in Protoplanetary Disks with Sulfur Molecules

Romane Le Gal[1,2,3,4,21], Karin I. Öberg[1], Richard Teague[1], Ryan A. Loomis[5], Charles J. Law[1], Catherine Walsh[6], Edwin A. Bergin[7], François Ménard[3], David J. Wilner[1], Sean M. Andrews[1], Yuri Aikawa[8], Alice S. Booth[6,9], Gianni Cataldi[8,10], Jennifer B. Bergner[11,22], Arthur D. Bosman[7], L. Ilse Cleeves[12], Ian Czekala[13,14,15,16,17,22], Kenji Furuya[10], Viviana V. Guzmán[18], Jane Huang[1,7,22], John D. Ilee[6], Hideko Nomura[10], Chunhua Qi[1], Kamber R. Schwarz[19,22], Takashi Tsukagoshi[10], Yoshihide Yamato[8], and Ke Zhang[7,20,23]

[1] Center for Astrophysics | Harvard & Smithsonian, 60 Garden St., Cambridge, MA 02138, USA; Romane.Le-Gal@univ-grenoble-alpes.fr
[2] IRAP, Université de Toulouse, CNRS, CNES, UT3, F-31000 Toulouse, France
[3] Université Grenoble Alpes, CNRS, IPAG, F-38000 Grenoble, France
[4] IRAM, 300 rue de la Piscine, F-38406 Saint-Martin d'Hères, France
[5] National Radio Astronomy Observatory, Charlottesville, VA 22903, USA
[6] School of Physics and Astronomy, University of Leeds, Leeds, LS2 9JT, UK
[7] Department of Astronomy, University of Michigan, 323 West Hall, 1085 S. University Avenue, Ann Arbor, MI 48109, USA
[8] Department of Astronomy, Graduate School of Science, The University of Tokyo, 7-3-1 Hongo, Bunkyo-ku, Tokyo 113-0033, Japan
[9] Leiden Observatory, Leiden University, 2300 RA Leiden, The Netherlands
[10] National Astronomical Observatory of Japan, 2-21-1 Osawa, Mitaka, Tokyo 181-8588, Japan
[11] University of Chicago Department of the Geophysical Sciences, Chicago, IL 60637, USA
[12] University of Virginia, Charlottesville, VA 22903, USA
[13] Department of Astronomy and Astrophysics, 525 Davey Laboratory, The Pennsylvania State University, University Park, PA 16802, USA
[14] Center for Exoplanets and Habitable Worlds, 525 Davey Laboratory, The Pennsylvania State University, University Park, PA 16802, USA
[15] Center for Astrostatistics, 525 Davey Laboratory, The Pennsylvania State University, University Park, PA 16802, USA
[16] Institute for Computational & Data Sciences, The Pennsylvania State University, University Park, PA 16802, USA
[17] Department of Astronomy, 501 Campbell Hall, University of California, Berkeley, CA 94720-3411, USA
[18] Instituto de Astrofísica, Pontificia Universidad Católica de Chile, Av. Vicuña Mackenna 4860, 7820436 Macul, Santiago, Chile
[19] Lunar and Planetary Laboratory, University of Arizona, 1629 E. University Blvd., Tucson, AZ 85721, USA
[20] Department of Astronomy, University of Wisconsin−Madison, 475 N. Charter St., Madison, WI 53706, USA
Received 2021 February 23; revised 2021 September 10; accepted 2021 September 10; published 2021 November 3

Abstract

Sulfur-bearing molecules play an important role in prebiotic chemistry and planet habitability. They are also proposed probes of chemical ages, elemental C/O ratio, and grain chemistry processing. Commonly detected in diverse astrophysical objects, including the solar system, their distribution and chemistry remain, however, largely unknown in planet-forming disks. We present CS (2 − 1) observations at ∼0.″3 resolution performed within the ALMA MAPS Large Program toward the five disks around IM Lup, GM Aur, AS 209, HD 163296, and MWC 480. CS is detected in all five disks, displaying a variety of radial intensity profiles and spatial distributions across the sample, including intriguing apparent azimuthal asymmetries. Transitions of C_2S and SO were also serendipitously covered, but only upper limits are found. For MWC 480, we present complementary ALMA observations at ∼0.″5 of CS, ^{13}CS, C^{34}S, H_2CS, OCS, and SO_2. We find a column density ratio $N(H_2CS)/N(CS) \sim 2/3$, suggesting that a substantial part of the sulfur reservoir in disks is in organic form (i.e., $C_xH_yS_z$). Using astrochemical disk modeling tuned to MWC 480, we demonstrate that $N(CS)/N(SO)$ is a promising probe for the elemental C/O ratio. The comparison with the observations provides a supersolar C/O. We also find a depleted gas-phase S/H ratio, suggesting either that part of the sulfur reservoir is locked in solid phase or that it remains in an unidentified gas-phase reservoir. This paper is part of the MAPS special issue of the Astrophysical Journal Supplement.

Unified Astronomy Thesaurus concepts: Protoplanetary disks (1300); Planet formation (1241); Interstellar molecules (849); Radio astronomy (1338); Interferometry (808); Astronomical models (86); Chemical abundances (224); Interstellar abundances (832); Astrochemistry (75)

1. Introduction

Protoplanetary disks are a pivotal stage in the evolution from interstellar molecular clouds to planetary systems. Their chemical structures encode information both on the chemical evolution during star and planet formation and on the future composition of planets. It is thus of fundamental importance to constrain and understand the chemistry of the principal chemical elements constituting these disks. During the past decade, a myriad of studies focused on oxygen, carbon, and nitrogen chemistry in protoplanetary disks (e.g., Öberg et al. 2011; Guilloteau et al. 2016; Cleeves et al. 2018; Kastner et al. 2018; Bergner et al. 2018, 2019; Pontoppidan et al. 2019), while very little is known about sulfur chemistry in disks. This is probably because, more generally, the chemistry of sulfur in the universe has remained a long-standing mystery for the past two decades (Ruffle et al. 1999; Kama et al. 2019; Navarro-Almaida et al. 2020).

Sulfur plays an important role in prebiotic chemistry (Chen et al. 2015) and planet habitability (Ranjan et al. 2018; Ruf et al. 2019). It is also one of the most abundant elements in the

[21] CNES Fellowship Program Fellow.
[22] NASA Hubble Fellowship Program Sagan Fellow.
[23] NASA Hubble Fellow.

universe, with a solar value of $S/H \sim 1.5 \times 10^{-5}$ (Asplund et al. 2009). In the diffuse interstellar medium (ISM) and photodissociation regions (PDRs) the total amount of sulfur is close to the solar value (Goicoechea et al. 2006; Howk et al. 2006), while in dense molecular gas it is strongly depleted: less than ∼1% of the sulfur solar abundance is observed in the gas phase (Tieftrunk et al. 1994; Wakelam et al. 2004; Vastel et al. 2018). Therefore, a question yet to be answered is, what causes the observed sulfur depletion from diffuse to dense gas? While most of the sulfur is suspected to be locked into icy grain mantles (e.g., Millar & Herbst 1990; Ruffle et al. 1999; Vidal et al. 2017; Laas & Caselli 2019), only ∼4% of the solar S abundance has been detected in interstellar ices so far (Palumbo et al. 1997; Boogert et al. 2015). Therefore, the identity of the sulfur reservoir(s) in the ISM remains an open question.

In the solar system, sulfur-bearing species are routinely detected in the remnants of our own planet-forming disk such as comets and meteorites, and on planets and their satellites (e.g., Calmonte et al. 2016; Hirschmann 2016; Lellouch et al. 2007; Franz et al. 2019). In particular, in comets, a dozen S-bearing species have now been detected (Meier & A'Hearn 1997; Bockelée-Morvan et al. 2004; Biver et al. 2016; Calmonte et al. 2016), including both complex S molecules (CH_3SH and C_2H_6S[24]) and multisulfuretted molecules, such as S_2, CS_2, S_3, and S_4, which have not been detected yet in the ISM or in protoplanetary disks. Studying the S chemistry in disks is therefore crucial to understand the chemical origins of our own solar system and, more generally, the role of sulfur in astrochemistry.

Among the approximately 30 different molecules detected in disks so far, only five contain sulfur.[25] These include CS, SO, H_2S, H_2CS, and SO_2, with the first two detected during the past two decades and the last three detected within the past few years owing to the significant sensitivity improvements made in radio interferometry instruments. CS is the most readily detected S-bearing species in protoplanetary disks (Dutrey et al. 1997; Fuente et al. 2010; Guilloteau et al. 2016; Teague et al. 2018b; Le Gal et al. 2019b). SO was the sole oxygenated, sulfur-bearing species detected in disks until the recent detection of SO_2 in one disk (Booth et al. 2021), which is probably indicative of a general highly reduced or O-poor gas chemistry in most disks. Another interesting point is that, so far, SO has only been detected toward a few young disks with signs of active accretion (Fuente et al. 2010; Guilloteau et al. 2013, 2016; Pacheco-Vázquez et al. 2016; Booth et al. 2018; Rivière-Marichalar et al. 2020). H_2S has long been thought to be a main sulfur reservoir and is a major sulfur carrier in comet 67P/C-G (Calmonte et al. 2016). However, it was only detected recently in the massive disk (∼0.15 $M_\odot$) GG Tau, with an H_2S/CS gas-phase column density ratio of $\sim 1/20$ (Phuong et al. 2018), after unsuccessful searches in a handful of other disks (GO Tau, MWC 480, DM Tau, and LkCa 15; Dutrey et al. 2011). While additional H_2S observations in disks are required to draw firm conclusions, this result casts doubt on the importance of H_2S in disk gas-phase S chemistry and has revived interest in the quest to identify the sulfur reservoir in disks (e.g., Kama et al. 2019). The recent detection of H_2CS in the MWC 480 disk, with an H_2CS/CS gas-phase column density ratio of $\sim 1/3$, is in tension with recent models (Le Gal et al. 2019b) and suggests an incomplete theoretical understanding of disk S chemistry. Thus, a better understanding of the S chemistry is needed to inform astrochemical models and constrain the unseen reservoirs of S-bearing species, such as those locked onto icy dust grains, in disks.

Disks are vertically stratified into atmospheres, warm molecular layers, and cold midplanes, which are analogs to PDR, lukewarm molecular clouds, and cold dense cores, respectively (Aikawa et al. 2002; Bergin et al. 2007; Dutrey et al. 2014). Recent sulfur-bearing species observations in each of these three types of astrophysical environments—i.e., in a PDR (Fuente et al. 2017; Rivière-Marichalar et al. 2019), in a protostellar envelope (Drozdovskaya et al. 2018) and in dense cores (Vastel et al. 2018; Navarro-Almaida et al. 2020)—have revived interest in the global quest for understanding the cycle of sulfur chemistry from molecular cloud to exoplanetary systems and are timely for disk S chemistry exploration. In this context, Le Gal et al. (2019b) scrutinized the reactions pertinent to the sulfur chemistry within current gas-grain astrochemical models to constrain those molecules expected to be particularly abundant in disks, and they predicted their radial and vertical distributions.

Here we present new observations of sulfur-bearing species in disks taken with the Atacama Large Millimeter/submillimeter Array (ALMA), as part of the Molecules with ALMA at Planet-forming Scales (MAPS) Large Program (Öberg et al. 2021). The ^{12}CS $J = 2 - 1$ rotational transition was observed toward the five disks targeted within MAPS, i.e., the disks orbiting IM Lup, GM Aur, AS 209, HD 163296, and MWC 480 (for which stellar and disk properties are described in Table 1). The SO $J_N = 2_3 - 1_2$ and $J_N = 5_4 - 4_4$ and C_2S $J_N = 8_7 - 7_6$ and $J_N = 15_{14} - 14_{15}$ rotational transitions were also serendipitously covered. In addition, we also present new complementary Cycle 6 ALMA observations (program 2018.1.01631.S; PI: R. Le Gal) toward the MWC 480 disk, where ^{12}CS $J = 5 - 4$ and its ^{13}CS and $C^{34}S$ isotopologues were observed, as well as several rotational transitions of H_2CS, OCS, and SO_2.

The outline of the paper is as follows: we describe the observations in Section 2, and we present the results, including the derivation of column densities and excitation temperatures, in Section 3. In Section 4, we present grids of disk chemistry models tuned to the MWC 480 disk, where we obtained the most observational constraints. In Section 5, we discuss the observational and modeling results, and we summarize our conclusions in Section 6.

2. Observations

We used three sets of ALMA observational data. First, new observations obtained with MAPS (program No. 2018.1.01055.L, PI: K. Öberg) of the ^{12}CS $2 - 1$ rotational transition and of two rotational transitions of SO and C_2S that were serendipitously covered in the same program. Second, new observations were obtained with another ALMA program (program No. 2018.1.01631.S, PI: R. Le Gal) of CS, ^{13}CS, and $C^{34}S$ $5 - 4$, four H_2CS rotational transitions, two OCS rotational transitions, and three SO_2 rotational transitions. Finally, to get better estimates of the column densities and excitation temperatures

[24] Note that C_2H_6S has two isomers, ethanethiol (CH_3CH_2SH, also known as ethyl mercaptan and only detected in Orion KL so far; Kolesniková et al. 2014) and dimethyl sulfide ($(CH_3)_2S$, which is, to our knowledge, not yet detected elsewhere in space). However, the 67P/C-G measurements did not allow us to distinguish the ratio of these two isomers.

[25] For this inventory we did not include isotopologues, but note that the isotopologues ^{13}CS and $C^{34}S$ are also detected in disks (Le Gal et al. 2019b; Loomis et al. 2020).

Table 1
Stellar and Disk Properties as Presented in Öberg et al. (2021)

Source	Spectral Type	Dist. (pc)	Incl (deg)	PA (deg)	$T_{\rm eff}$ (K)	L_* ($L_\odot$)	Age[a] (Myr)	M_*[b] ($M_\odot$)	$\log_{10}(\dot{M})$ ($M_\odot$ yr^{-1})	$v_{\rm sys}$ (km s^{-1})	References
IM Lup	K5	158	47.5	144.5	4266	2.57	∼1	1.1	−7.9	4.5	1,2,3,4,5,6
GM Aur	K6	159	53.2	57.2	4350	1.2	∼3–10	1.1	−8.1	5.6	1,7,8,9,10,11,12
AS 209	K5	121	35.0	85.8	4266	1.41	∼1–2	1.2	−7.3	4.6	1,2,6,13,14
HD 162396	A1	101	46.7	133.3	9332	17.0	$\gtrsim$6	2.0	−7.4	5.8	1,2,6,15,16
MWC 480	A5	162	37.0	148.0	8250	21.9	∼7	2.1	−6.9	5.1	1,17,18,19,20,21

References. (1) Gaia Collaboration et al. 2018; (2) Huang et al. 2018; (3) Alcalá et al. 2017; (4) Pinte et al. 2018; (5) Mawet et al. 2012; (6) Andrews et al. 2018; (7) Huang et al. 2020; (8) Macías et al. 2018; (9) Espaillat et al. 2010; (10) Kraus & Hillenbrand 2009; (11) Beck & Bary 2019; (12) Ingleby et al. 2015; (13) Salyk et al. 2013; (14) Huang et al. 2017; (15) Fairlamb et al. 2015; (16) Teague et al. 2019; (17) Liu et al. 2019; (18) Montesinos et al. 2009; (19) Simon et al. 2019; (20) Piétu et al. 2007; (21) Mendigutía et al. 2013.

[a] The stellar ages are uncertain by at least a factor of two and should only be considered as preliminary estimates.

[b] All stellar masses have been dynamically determined as described in Teague et al. (2021).

of H_2CS, ^{12}CS, and $C^{34}S$, we also used already-published complementary ALMA data of additional detected rotational transitions of these molecules (Le Gal et al. 2019b). The new observations are further described below, and their molecular transitions, frequencies, and spectroscopic parameters are listed in Table 2.

2.1. MAPS Observations

The CS $2-1$ rotational transition was observed in the five MAPS disks in Band 3 with an angular resolution of $\sim 0\farcs3$ (see Table 2) and a spectral resolution of 71 kHz, corresponding to $\sim$0.22 km s^{-1} at 97 GHz. More details about the observations can be found in Öberg et al. (2021). For the descriptions of the reduction and imaging procedures applied to the CS $2-1$ MAPS observations, we refer the reader to Öberg et al. (2021) and Czekala et al. (2021), respectively. Here we used the CS $2-1$ images created with a robustness parameter of 0.5 for the Briggs weighting, which results in slightly higher resolution images than the fiducial images presented in Öberg et al. (2021) and Law et al. (2021), which used circularized $0\farcs3$ beams.

While SO and C_2S were not part of the main targeted molecules within the MAPS program, two of their rotational transitions—namely, the 2_3-1_2 (at 99.29987 GHz) and 5_4-4_4 (at 100.02964 GHz) transitions for SO and the 8_7-7_6 (at 99.86652 GHz) and $15_{14}-14_{15}$ (at 234.81596 GHz) lines for C_2S—were covered in Bands 3 and 6, at lower spectral resolution (1.129 MHz, i.e., $\sim$3.4 km s^{-1} at 100 GHz and $\sim$1.4 km s^{-1} at 235 GHz). After continuum subtraction with the CASA `uvcontsub` function, we `CLEAN`ed (Högbom 1974) the C_2S and SO data using the same procedure as outlined in Czekala et al. (2021). As these lines are expected to be weak, we applied a robustness parameter of 1 and $1''$ *uv*-taper to improve their imaging and signal-to-noise ratio (S/N). All MAPS images used here are available for download through the ALMA Archive via https://almascience.nrao.edu/alma-data/lp/maps. An interactive browser for this repository is also available on the MAPS project homepage at http://www.alma-maps.info.

2.2. Complementary ALMA Observations of MWC 480

Independently from the MAPS program, Cycle 6 ALMA observations toward the MWC 480 disk were conducted on 2019 April 30 in three execution blocks (EBs) with an angular resolution of $\sim 0\farcs55$, as part of program 2018.1.01631.S (PI: R. Le Gal). We are presenting and using these data here to complement the data set of sulfur-bearing molecules observed for this disk. The measurements used ALMA Band 6 receivers, with correlated data divided into 13 spectral windows (SPWs). SPWs were centered on 12 different rotational transitions of sulfur-bearing molecules, including the CS, ^{13}CS, and $C^{34}S$ $5-4$ lines; four H_2CS lines; two OCS lines; and three SO_2 lines. Each SPW contains 480 channels with a total bandwidth of 58.59 MHz, with a 0.141 MHz resolution per channel, corresponding to a velocity resolution of $\sim$0.18 km s^{-1}. One SPW was reserved for high-sensitivity continuum observations to aid in the self-calibration of the data. The total on-source integration time was $\sim$43 minutes. A total of 42 and 43 antennas were included for the first EB and the remaining two EBs, respectively, and covered baselines from 15 to 740 m. All EBs used the source J0510+1800 as their bandpass and flux calibrators and the source J0438+3004 as phase calibrator. Only one-third of the proposed observations were performed, and both the rms and beam size failed to meet our requested performance parameters. Therefore, the observations were deemed to QA2 SEMI-PASS and the data released by the observatory. However, the data quality already allows us to derive constraints on the S chemistry as described below.

Data calibration was initially pipeline processed. We then use the Common Astronomy Software Application package (CASA) version CASA 5.6.1–8 (McMullin et al. 2007) to reduce the data. Self-calibration was performed using the SPW reserved for continuum. We performed three iterations of phase self-calibrations and then one amplitude self-calibration. After continuum subtraction with the CASA `uvcontsub` function, the data were `CLEAN`ed (Högbom 1974) using 3σ noise threshold and Briggs weighting with a robustness parameter of 0.5 for the main CS isotopologue and of 1 with a taper of $1''$ for the other lines to improve their imaging and S/N. The values of rms per channel of all the observations presented in this study are listed in Table 2.

3. Observational Results

3.1. CS $2-1$ Fluxes and Spatial Distributions

Figure 1 displays the integrated intensity (zeroth-moment) maps of the spatially resolved MAPS observations of the CS $2-1$ rotational transition toward each of the five targeted disks. To build these maps, we used the Python package `bettermoments` (Teague & Foreman-Mackey 2018) applied

Table 2
List of Observations (Molecular Data from CDMS[a])

Species	Transition	Frequency (GHz)	E_u (K)	$\mathrm{Log}_{10}(A_{ij})$ (s^{-1})	Source	rms_{chan} (mJy $beam^{-1}$)	Restored Beam (arcsec × arcsec)	Restored Beam (deg)	R_{max}[b] (arcsec)	$S_\nu\Delta_\nu(R_{max})$[c] (mJy km s^{-1})
MAPS data (Project ID: 2018.1.01055.L)										
^{12}CS	$2-1$	97.98095	7.1	−4.7763	IM Lup	0.51	0.30×0.23	−80.2	3.0 ± 0.1	268 ± 11
					GM Aur	0.46	0.39×0.27	5.1	2.1 ± 0.1	133 ± 3
					AS 209	0.48	0.33×0.26	−66.7	0.9 ± 0.1	166 ± 4
					HD 163296	0.42	0.31×0.24	−88.2	1.5 ± 0.1	302 ± 15
					MWC 480	0.46	0.39×0.28	7.2	2.0 ± 0.1	48 ± 4
SO	2_3-1_2	99.29987	9.2	−4.9488	IM Lup	0.44	1.23×1.12	79.3	3.0 ± 0.1	$\lesssim 30$
					GM Aur	0.42	1.44×1.29	−5.9	2.1 ± 0.1	<10
					AS 209	0.40	1.33×1.11	82.7	0.9 ± 0.1	<15
					HD 163296	0.39	1.22×1.05	85.3	1.5 ± 0.1	<45
					MWC 480	0.43	1.44×1.29	−3.6	1.5 ± 0.2	$\lesssim 14$
	5_4-4_4	100.02964	38.6	−5.9656	IM Lup	0.50	1.22×1.09	82.1	3.0 ± 0.1	<51
					GM Aur	0.45	2.10×1.37	−29.0	2.1 ± 0.1	$\lesssim 4$
					AS 209	0.41	1.28×1.10	−80.9	0.9 ± 0.1	<18
					HD 163296	0.41	1.26×1.07	85.0	1.5 ± 0.1	<53
					MWC 480	0.41	2.08×1.38	−28.8	1.5 ± 0.2	<6
C_2S	8_7-7_6	99.86652	28.1	−4.3562	IM Lup	0.49	1.22×1.09	82.1	3.0 ± 0.1	<51
					GM Aur	0.45	2.10×1.37	−29.0	2.1 ± 0.1	<9
					AS 209	0.41	1.29×1.10	−80.9	0.9 ± 0.1	$\lesssim 9$
					HD 163296	0.39	1.26×1.07	85.0	1.5 ± 0.1	<53
					MWC 480	0.48	2.08×1.38	−28.8	1.5 ± 0.2	<5
Complementary Cycle 6 Unpublished ALMA data (Project ID: 2018.1.01631.S)										
^{12}CS	$5-4$	244.93564	35.3	−3.5271	MWC 480	3.9	0.71×0.45	−12.9	1.5 ± 0.2	98 ± 5
^{13}CS	$5-4$	231.22010	33.3	−3.6008	MWC 480	4.4	0.83×0.58	0.7	1.5 ± 0.2	<7
$C^{34}S$	$5-4$	241.01609	27.8	−3.5568	MWC 480	3.4	0.86×0.59	6.8	1.5 ± 0.2	20 ± 5
H_2CS	$7_{16}-6_{15}$	244.04850	60.0	−3.6771	MWC 480	3.2	0.79×0.55	1.0	1.5 ± 0.2	29 ± 5
	$7_{26}-6_{25}$	240.38205	98.8	−3.7248		3.9	0.87×0.59	6.8		<13
	$7_{35}-6_{34}$	240.39304	164.6	−3.7760		4.0	0.86×0.59	6.3		<10
	$7_{34}-6_{33}$	240.39376	164.6	−3.7760		4.0	0.86×0.59	6.3		<10
OCS	$19-18$	231.06099	110.9	−4.4463	MWC 480	3.3	0.78×0.54	−0.02	1.5 ± 0.2	<5
	$20-19$	243.21804	122.6	−4.3790		3.0	0.79×0.55	0.76		<13
SO_2	$11_{57}-12_{48}$	229.34763	122	−4.7194	MWC 480	2.7	0.84×0.58	1.4	1.5 ± 0.2	18 ± 6
	$5_{24}-4_{13}$	241.61580	23.6	−4.0728		3.2	0.86×0.59	5.9		<6
	$5_{42}-6_{33}$	243.08765	53.1	−4.9886		2.9	0.79×0.55	1.2		<6

Notes.
[a] https://cdms.astro.uni-koeln.de/cdms/portal/; Müller et al. (2001, 2005).
[b] R_{max} stands for the outer radius of the molecular line emission, where 90% of the cumulative flux from the radial profiles is contained. The uncertainty is 1σ error.
[c] $S_\nu\Delta_\nu(R_{max})$ corresponds to the flux density integrated out to the outer radius R_{max} of the molecular line emission.

to the image cube available for download in the MAPS data repository. We used a hybrid mask combining a Keplerian mask (also available for download in the MAPS data repository) and 3σ clip to mask any pixels below this threshold. For comparison, we also show the 3 mm continuum emission maps made in Sierra et al. (2021). Radially deprojected and azimuthally averaged intensity profiles of the continuum and CS $2-1$ line are also shown for each of the five MAPS disks. These were produced using the `radial profile` function of the Python package `GoFish` (Teague 2019), considering the disk physical parameters (i.e., disk inclination, disk position angle, mass of the central star, and distance) listed in Table 1. The angular resolution is $\sim 0\farcs3$, i.e., ranging from 30 au (HD 163296) to 49 au (MWC 480) depending on distance across the sample of MAPS disks. Finally, the CS $2-1$ spectra are also depicted in Figure 1 for each targeted disk, showing a typical double-peaked profile indicative of the Keplerian rotation of the disk.

Based on the radial intensity profiles of the CS $2-1$ emission across the disk sample, central holes appear for IM Lup and HD 163296, with the largest radial hole extent found toward HD 163296. For the other three disks, the S/N and spatial resolution are not sufficient to infer the morphology of the inner disk emission. Beyond the inner holes we see a wide diversity in the morphology and extent of the CS $2-1$ radial intensity profiles compared to the dust continuum. For instance, emission plateaus appear for IM Lup, GM Aur, and HD 163296, leading to outer CS $2-1$ emission radii a factor of ≈ 2 larger than the dust continuum. The GM Aur disk—the only transition disk in the MAPS sample—is the only disk in

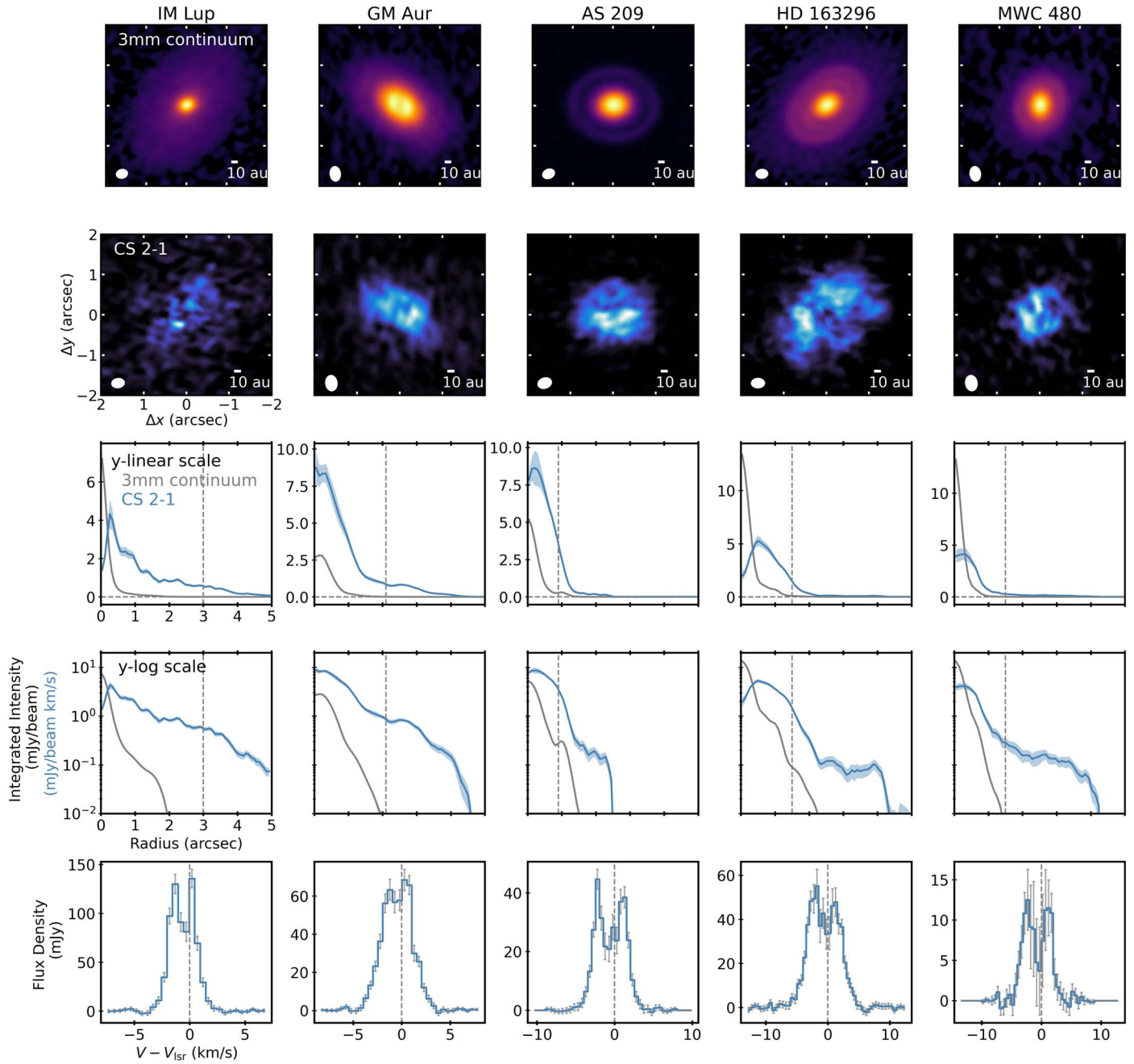

Figure 1. Zeroth-moment maps and radial intensity profiles for the MAPS disk sample, ordered by increasing stellar mass (see Table 1), from left to right. First row: zeroth-moment maps of the dust continuum at 3 mm produced using an arcsinh color stretch for the AS 209 disk, and a power-law color stretch for all four other disks, to enhance the faint and extended emission. Second row: zeroth-moment maps of CS 2 − 1. Synthesized beams are shown in the lower left corner of each panel. Third and fourth rows: radially deprojected and azimuthally averaged intensity profiles of the continuum and the CS 2 − 1 emission in y-linear and y-log scales, respectively. The vertical dashed gray lines indicate the outer radius R_{max} of the molecular line emission, where 90% of the cumulative flux from the radial profiles is contained within 1σ error. Fifth row: integrated intensity spectra of CS 2 − 1. The uncertainties on radial and intensity profiles are calculated as the standard deviation on the mean in the radial annulus over which the emission was averaged, following the MAPS collaboration convention, described in detail in Law et al. (2021). Hence, these error bars do not include the absolute calibration uncertainty of 10%.

which we see a tentative outer emission ring at $\sim 2\farcs5$ (i.e., $\sim$400 au).

Interestingly, the zeroth-moment maps of the CS $2-1$ emission show some asymmetries that do not appear in the dust emission. In particular, toward four of the sources (GM Aur, AS 209, HD 163296, and MWC 480), we find up to a factor of 2 or 5σ of intensity difference between the near and far sides of the disks. Since the five MAPS disks have a nonzero inclination (see Table 1), the closest and farthest half disk sides, with respect to the disk semimajor axis, are defined as near and far disk sides, respectively. This is illustrated by the schematic views of the geometry of each disk that we show as insets in Figure 2. For three of the five MAPS sources—namely, AS 209, HD 163296, and GM Aur—the brightest CS emission sides coincide with the near side of the disks. Intriguingly, the reverse is observed for MWC 480, where the brightest CS emission side coincides with the far side of the disk. However, given the relatively low S/N, the robustness of these

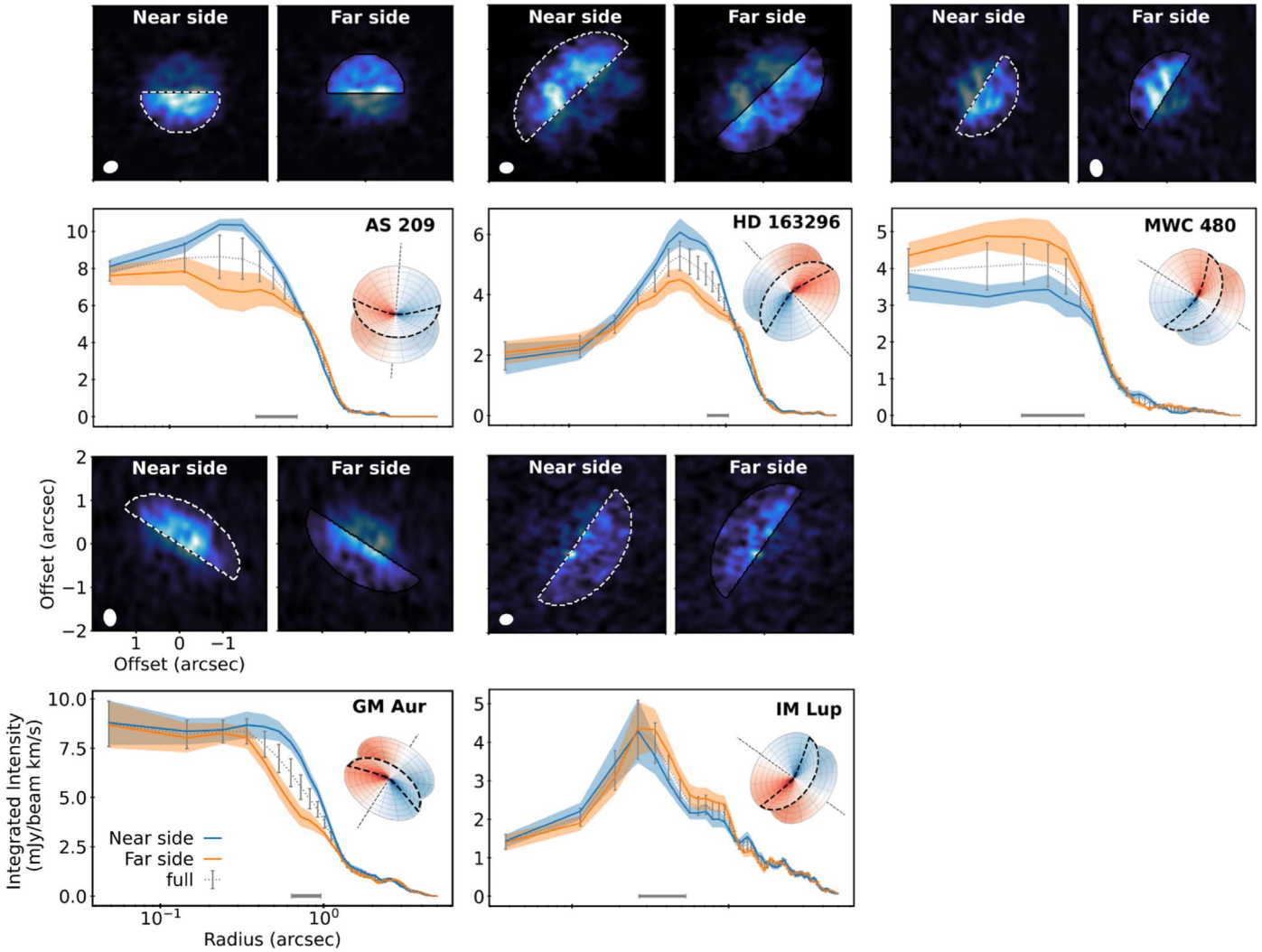

Figure 2. First and third rows: zeroth-moment maps of the CS 2 − 1 emission in the far and near sides of each of the five MAPS disks. Synthesized beams are shown in the lower left corner of the panels presenting the far side of each disk. Second and fourth rows: radially deprojected and averaged intensity profiles of the farthest (blue) and near (orange) CS 2 − 1 emission sides of each disk compared to the azimuthally averaged intensity profiles (gray dotted line). The uncertainties on the radial intensity profiles are calculated as the standard deviation on the mean in the radial annulus over which the emission was averaged. Synthesized beams are shown by the gray error bar below each radial intensity profile. The insets represent a schematic view of each disk inclination.

asymmetries is hard to assess. As for IM Lup, which is the disk with the smallest CS 2 − 1 integrated intensity, we do not observe such asymmetries. These asymmetries are further discussed in Section 5.4.

3.2. CS Isotopologues and H_2CS in MWC 480

The ^{13}CS and C^{34}S 5 − 4 rotational transitions were observed as part of our complementary ALMA program toward MWC 480 (see Section 2.2). We did not detect the ^{13}CS 5 − 4 line with either the matched filtering method (`VISIBLE`; Loomis et al. 2018b) or line velocity shift and stacking techniques (`GoFish`; Teague 2019). The latter exploits the known geometry and velocity structure of the disk to deproject the rotation profile and combine Doppler-shifted emission to a common centroid velocity reference frame. This results in a single disk-integrated spectrum for each transition. However, imaging the C^{34}S 5 − 4 line reveals a ∼3σ–4σ detection that is shown in Figure 3 and reported in Table 2. This detection is confirmed when we build the integrated spectrum of the line using the velocity shift and stacking methods of `GoFish` (see bottom panel in Figure 3). These results are consistent with the ^{13}CS and C^{34}S 6 − 5 observations reported in Le Gal et al. (2019b), where the C^{34}S line was tentatively detected toward the MWC 480 disk while ^{13}CS was not.

Four H_2CS transitions (see Table 2) were also observed as part of our complementary ALMA program toward the MWC 480 disk. Among these four transitions, only the H_2CS line with the lowest upper energy level (i.e., H_2CS $7_{16} - 6_{15}$) is detected, with a ∼5σ–6σ detection. The zeroth-moment map, the radially deprojected and azimuthally averaged intensity profile, and the shifted and stacked disk-integrated spectrum of the H_2CS $7_{16} - 6_{15}$ detection are shown in Figure 3. As for the remaining three H_2CS lines, their nondetections are not surprising regarding their upper energy levels and line strengths.

3.3. Multiline Analysis

To constrain the ^{12}CS, C^{34}S, and H_2CS column densities and excitation temperatures toward the MWC 480 disk, we combined the new observations presented here with complementary

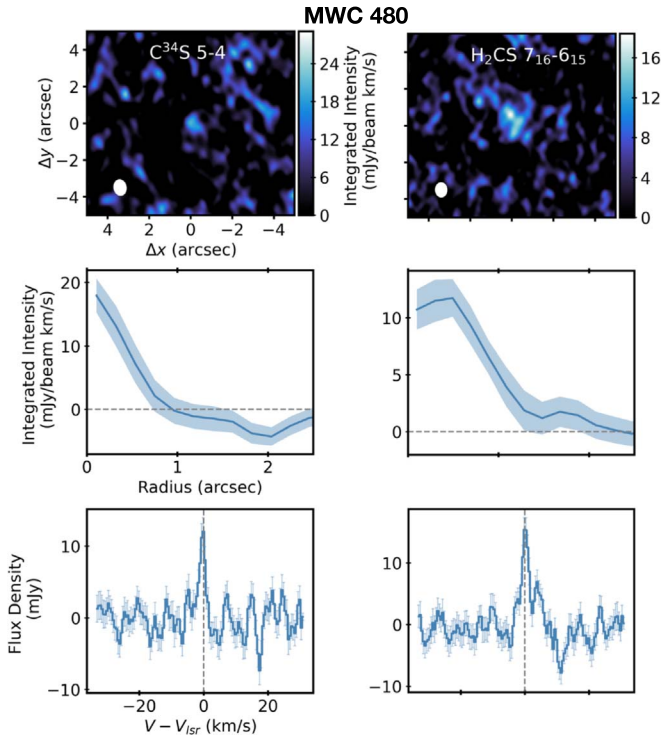

Figure 3. Zeroth-moment maps (top panels), radially deprojected and azimuthally averaged intensity profiles within 1σ, as in Figure 1 (middle panels), and shifted and stacked disk-integrated line spectra of the $C^{34}S$ $5-4$ (left) and H_2CS $7_{16}-6_{15}$ (right) rotational transitions observed toward the MWC 480 disk with 1σ (bottom panels). These last uncertainties are calculated on a per-channel basis, taking into account decorrelation along the spectral axis (see also Yen et al. 2016; Ilee et al. 2021).

ALMA observations of ^{12}CS ($5-4$ and $6-5$), $C^{34}S$ ($6-5$), and H_2CS ($8_{17}-7_{16}$, $9_{19}-8_{18}$, and $9_{18}-8_{17}$), already published in Le Gal et al. (2019b). Assuming optically thin lines and local thermal equilibrium (LTE), we used a rotational diagram analysis (Goldsmith & Langer 1999) to derive the disk-integrated column densities and excitation temperatures of these molecules. These quantities are derived from the disk-integrated flux densities, as described in Le Gal et al. (2019b) and summarized below.

To illustrate that the LTE assumption is justified, we show in Figure 4 the profiles of the main physical parameters used to build the MWC 480 disk physical structure, along with the number density computed for CS and H_2CS with our corresponding published model (Le Gal et al. 2019b). This allows us to show that the gas density in the main emitting molecular layers is larger than $10^7\,cm^{-3}$, i.e., well above the critical densities of the observed CS and H_2CS transitions, which justifies well the LTE assumption. For temperatures in the range $20-50$ K, the critical densities are in the range $\sim 7\times10^4-3\times10^6\,cm^{-3}$ for CS (Shirley 2015) and in the range $(2-4)\times10^6\,cm^{-3}$ for H_2CS, using scaled H_2CO collisional rates from Wiesenfeld & Faure (2013) (see the `Leiden Atomic and Molecular Database (LAMDA)`;[26] van der Tak et al. 2020).

Assuming optically thin transitions, the disk-integrated flux densities $S_\nu\Delta v$ can be related to the column density of their respective upper energy state, N_u, as follows:

$$N_u = \frac{4\pi S_\nu \Delta v}{A_{ul}\Omega hc}, \quad (1)$$

where S_ν is the flux density, Δv the line width, A_{ul} the Einstein coefficient, c the speed of light, and Ω the solid angle subtended by the source (e.g., Bisschop et al. 2008; Loomis et al. 2018a). For this analysis, we use the disk flux densities $S_\nu\Delta v$ integrated out to the outer radius of the molecular line emission, referred to as R_{max} in Table 2.

The disk-integrated column density, N_{tot}, and excitation temperature, T, can then be derived from the upper-level population, N_u, which follows the Boltzmann distribution:

$$N_{tot} = \frac{N_u}{g_u} Q_{rot}(T) e^{E_u/k_B T}, \quad (2)$$

with g_u and E_u the degeneracy and energy of the upper energy level u, respectively; k_B the Boltzmann constant; and Q_{rot} the partition function of the molecule, which for a diatomic molecule such as CS can be approximated by

$$Q_{rot}(T) \approx \frac{k_B\,T}{h\,B_0} + \frac{1}{3}. \quad (3)$$

In this expression h is the Planck constant and B_0 is the rotational constant of the molecule. For CS we used $B_0 = 24495.562\times10^6$ Hz (see CDMS). For H_2CS we interpolated the $\{T, Q_{rot}(T)\}$ values provided by CDMS.

Using Equation (2) and Appendix B of Le Gal et al. (2019b), the optical depth of a given transition at temperature T can be expressed as

$$\tau_\nu = \sqrt{\frac{4\ln 2}{\pi}} \frac{N_u A_{ul}\, c^3}{\Delta v_{FWHM}\, 8\pi\nu^3} (e^{h\nu/k_B T_{ex}} - 1), \quad (4)$$

where $\Delta v_{FWHM} = \sqrt{8\ln 2}\,\sigma_v$ is the FWHM of the observed transition; σ_v is the width of the Gaussian fit, since for optically thin lines the line profiles remain Gaussian.

As described in Appendix B of Le Gal et al. (2019b), we can substitute Equation (4) in $C_\tau = \frac{\tau}{1-e^{-\tau}}$, which corresponds to the "optical depth correction factor" for a square line profile in case $\tau \ll 1$ (Goldsmith & Langer 1999). This allows us to build a likelihood function $\mathcal{L}$(data, N_{tot}, T_{ex}) that we used with the Python implementation `emcee` (Foreman-Mackey et al. 2013) of the affine-invariant ensemble sampler for Markov Chain Monte Carlo (MCMC; Goodman & Weare 2010) to compute posterior probability distributions for T_{ex} and N_{tot}. The following uniform and permissive priors were assumed:

$$T_{ex}(K) = \mathcal{U}(3, 300) \quad (5)$$

$$N_{tot}(cm^{-2}) = \mathcal{U}(10^7, 10^{20}). \quad (6)$$

3.4. Disk-integrated Column Densities in MWC 480

Using the method described in Section 3.3, we derived the disk-integrated column densities of CS, $C^{34}S$, and H_2CS in MWC 480. The random draws from the posterior distributions for each molecule are depicted in gray in Figure 5. The uncertainties are derived from the median and 16th–84th percentiles of the posterior distributions, respectively. The 16th and 84th percentiles are chosen as equivalent to ±1 σ uncertainties on the fit. The results converged toward

[26] https://home.strw.leidenuniv.nl/~moldata/

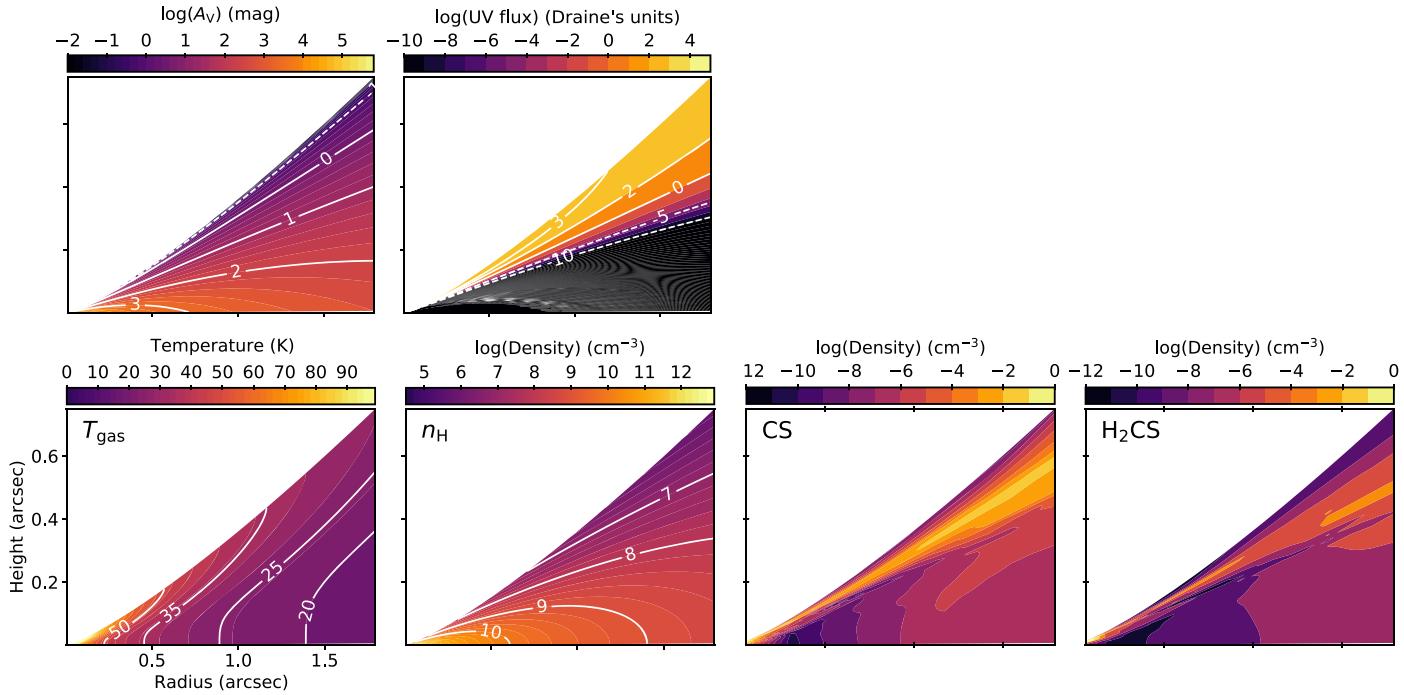

Figure 4. Top row: visual extinction and UV flux profiles fed in our MWC 480 protoplanetary disk astrochemical model (Le Gal et al. 2019b). Bottom row: the first two panels show the temperature and density 2D profiles fed in our MWC 480 protoplanetary disk astrochemical model. The third and fourth panels show the modeled number densities (i.e., absolute abundances) of CS and H_2CS. All panels are represented as functions of disk radius vs. height.

1. $T_{ex} \simeq 22.7^{+2.2}_{-1.8}$ K and $N_{tot} \simeq 6.2^{+0.5}_{-0.5} \times 10^{12}$ cm^{-2} for CS;
2. $T_{ex} \simeq 14.2^{+16.0}_{-6.8}$ K and $N_{tot} \simeq 6.9^{+15.6}_{-2.9} \times 10^{11}$ cm^{-2} for $C^{34}S$;
3. $T_{ex} \simeq 29.6^{+14.4}_{-8.6}$ K and $N_{tot} \simeq 4.0^{+2.1}_{-0.9} \times 10^{12}$ cm^{-2} for H_2CS.

This leads to $N(CS)/N(C^{34}S) \simeq 9^{+20}_{-3}$ and $N(CS)/N(H_2CS) \simeq 1.6^{+0.8}_{-0.4}$. While the uncertainties on the former do not allow us to draw any firm conclusion, the latter is about a factor of two lower than previously found using fewer rotational transitions with a smaller dynamic range in upper energy for H_2CS (i.e., here we have $E_u = 55.9$–88.5 K vs. $E_u = 73.4$–88.5 K in Le Gal et al. 2019b). This illustrates the need for multiple line observations for a given molecule, to better constrain its excitation temperature and column density with rotational diagram methods.

3.5. Radially Resolved Column Density of CS in MWC 480

Applying the same rotational diagram analysis to the radially deprojected and azimuthally averaged intensities, we compute the excitation temperature and column density of CS as a function of the distance from the star. All CS transitions were reimaged to have matching beam sizes (i.e., $\sim 0\farcs5$). The results are presented in Figure 6, along with the three CS lines' radial intensity profiles. They are in good agreement with the disk-integrated results, which are also depicted in Figure 6 to facilitate the comparison. As expected from the CS radial intensity profiles, the CS column density decreases with increasing radius. One can note that the disk average values appear biased toward small distances from the central star because the bulk of the emission is coming from these small distances. So this is why the radially resolved column densities are preferred when derivable. While the temperature gradient is consistent with typical earlier-derived radial temperature profiles, it is interesting to notice that the typical model temperatures are higher than the ones derived from the Boltzmann analysis of the observations.

3.6. Disk-integrated Column Density of CS in MAPS and Literature

Next, we estimate the disk-integrated CS column densities for the remaining four MAPS disks. As each of these disks only has a single CS transition observed with MAPS (i.e., $2-1$), we fix the excitation temperature to a minimum of 10 K and maximum of 30 K. This temperature range is based on the constraints derived for the MWC 480 disk (see Section 3.3), assuming that CS resides in similar temperature layers in each disk. We calculate the column densities associated with this temperature range using Equations (1) and (2). To enlarge our sample, we extended this calculation to another CS ALMA survey we performed in a sample of five additional disks (Le Gal et al. 2019b). The resulting CS disk-integrated column densities are shown in Figure 7, sorted by stellar mass. The CS disk-integrated column density varies by $\approx$1.5 orders of magnitude across the sample of disks, in the range of $\approx (0.2-6.0) \times 10^{13}$ cm^{-2}. There are no obvious trends with stellar mass or spectral type. The two Herbig Ae stars, MWC 480 and HD 163296, are close to the sample average.

3.7. Upper Limits and Tentative Detections of SO, C_2S, OCS, and SO_2

While the only sulfur-bearing molecular transition targeted in a dedicated SPW within MAPS was ^{12}CS $2-1$, transitions of C_2S and SO were covered within the MAPS program (see Table 2). Assuming Keplerian emission and using matched filtering (Loomis et al. 2018b), these lines were not detected. To check for non-Keplerian emission, we also imaged these lines using the Briggs weighting with a robust parameter of 1

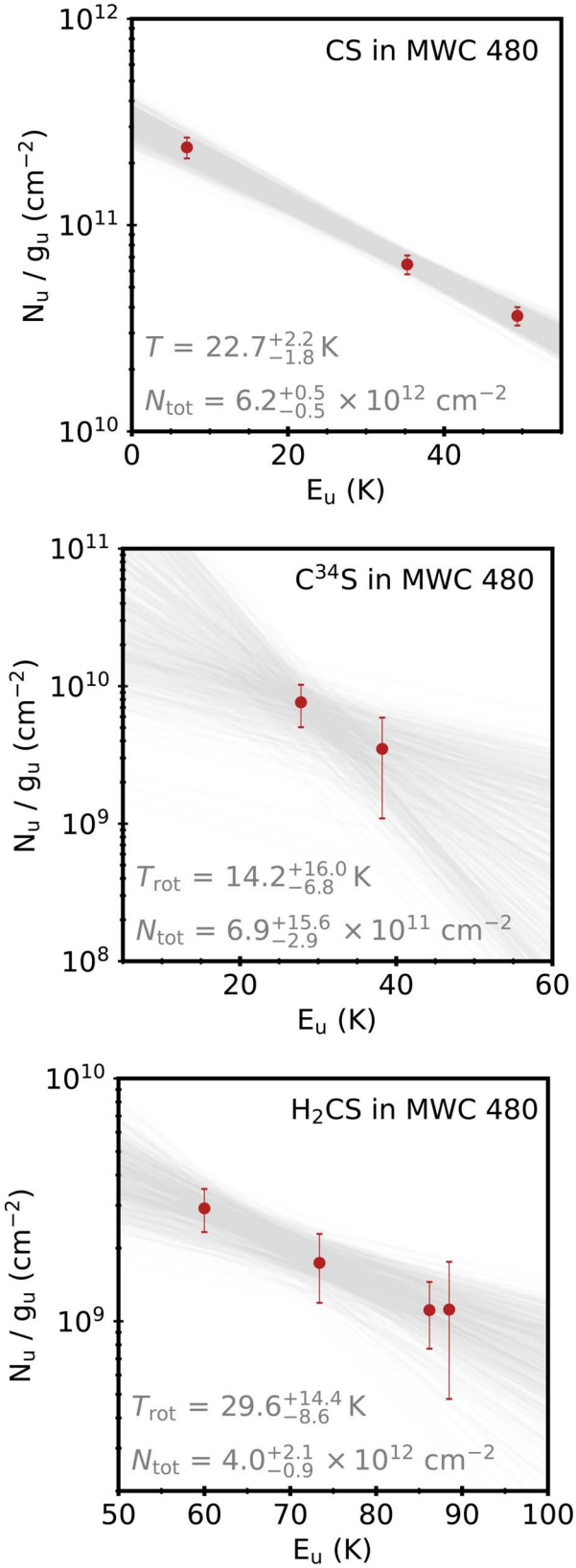

Figure 5. Rotational diagrams of the CS $2-1$, $5-4$, and $6-5$ rotational transitions (top panel); the $C^{34}S$ $5-4$ and $6-5$ rotational transitions (middle panel); and the H_2CS $7_{16}-6_{15}$, $8_{17}-7_{16}$, $9_{19}-8_{18}$, and $9_{18}-8_{17}$ rotational transitions (bottom panel), integrated over the outer radius of the molecular line emission, R_{max}, toward MWC 480. A 10% calibration uncertainty on the flux values is also included.

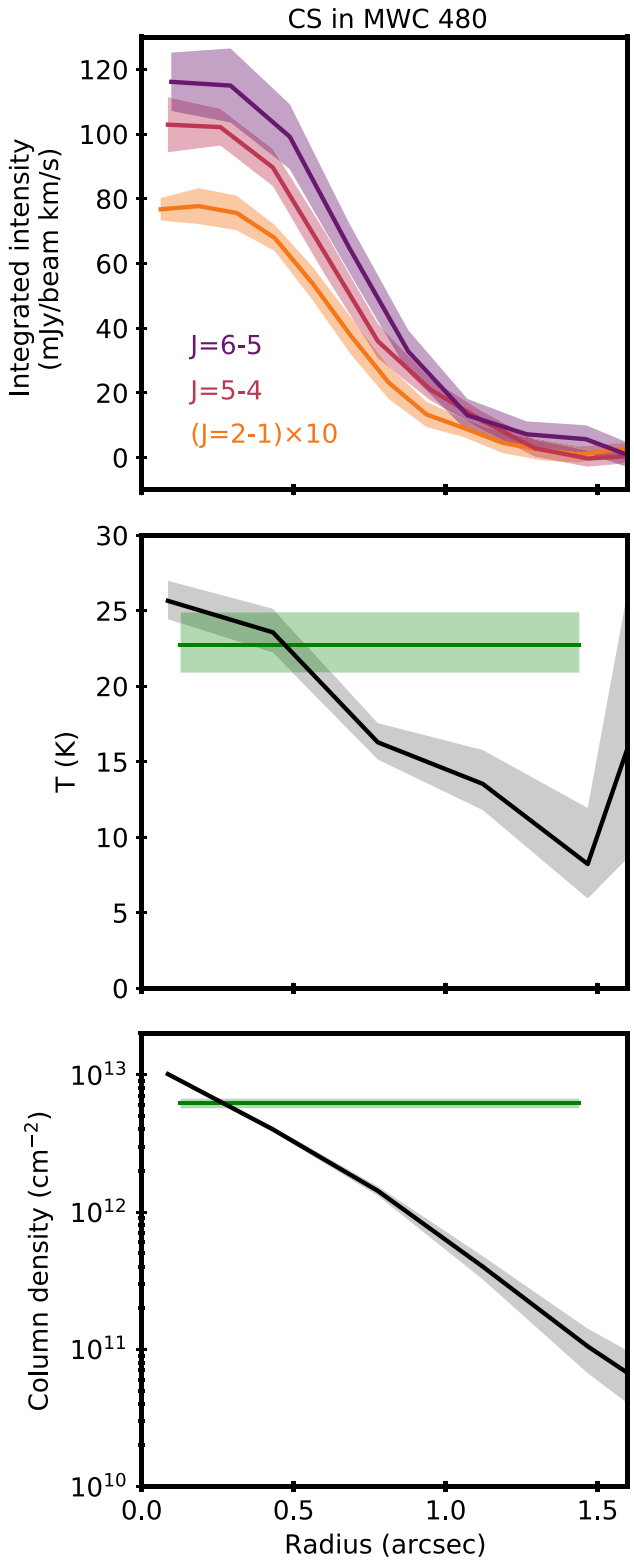

Figure 6. Top panel: radially deprojected and azimuthally averaged intensity profiles of the three rotational transitions CS $2-1$, $5-4$, and $6-5$ observed toward the MWC 480 disk. Middle and bottom panels: radially deprojected and azimuthally averaged excitation temperature and column density profiles of the MCMC rotational diagram results applied to the aforementioned three CS lines. Median values and uncertainties based on the 16th, 50th, and 84th percentiles of the samples are depicted. For comparison, the disk-integrated CS column density and excitation temperature are overplotted in green in the middle and bottom panels.

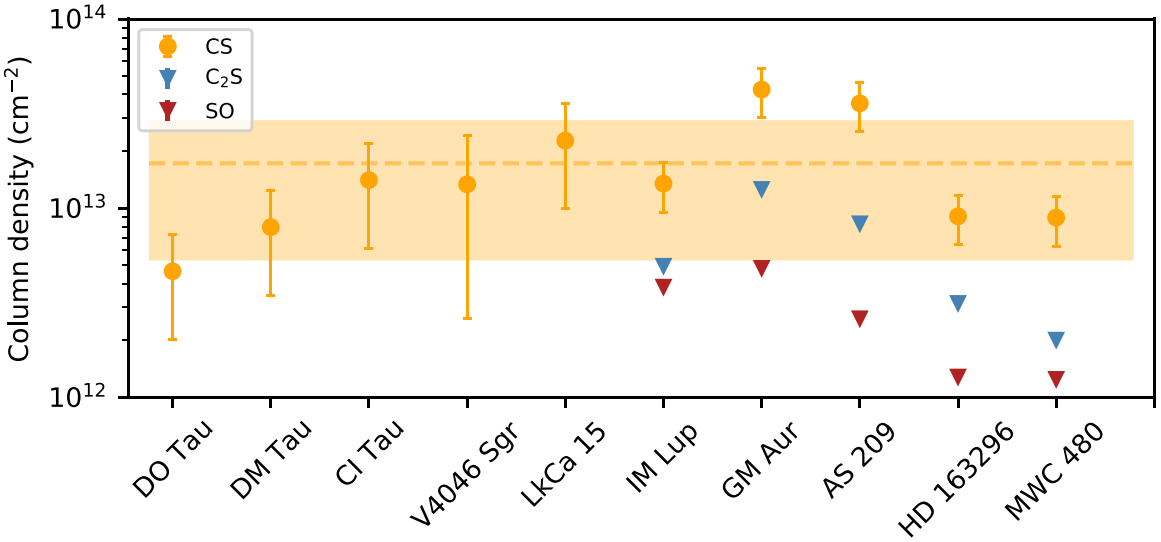

Figure 7. Estimated CS, SO, and C_2S column densities disk-integrated up to R_{max} for each MAPS disk (see Table 2) and computed for $T_{ex} = 10$–30 K. For CS, the disk sample is extended to the additional five disks surveyed in Le Gal et al. (2019b). The disks are sorted by increasing stellar mass. The averaged column density of CS is represented by the dashed orange line and its standard deviation by the orange rectangle. Upper limits are indicated by the downward-pointing triangles.

and a taper of 1″ to improve the S/N and image quality. The corresponding zeroth-moment maps and radially deprojected and azimuthally averaged intensity profiles are shown in the Appendix, in Figure A1. The integrated intensities and upper limits for the nondetections are reported in Table 2 for the corresponding ^{12}CS $2-1$ emitting area. To estimate the upper limits of the SO and C_2S column densities, we use Equations (1) and (2) with the constraints on the excitation temperature of CS derived in Section 3.3 (as done in Section 3.6). The results are overplotted in red and blue in Figure 7.

Finally, two other oxygenated sulfur-bearing molecules, SO_2 and OCS, were observed toward the MWC 480 disk, as part of our complementary ALMA program (see Table 2). Figure A2, in the Appendix, shows the zeroth-moment maps, radially deprojected and azimuthally averaged intensity profiles, and spectra of SO_2 and OCS, respectively. Integrating the intensity over the CS $2-1$ emitting area and FWHM, we find a 3σ tentative detection of SO_2 (see Table 2) that is also distinguishable from the zeroth-moment map, where we see a subtle flux peak toward the disk. However, we do not reproduce a detection when using matched filtering (implemented in `VISIBLE`), nor with velocity shifting and stacking (implemented in `GoFish`). As for OCS, it is not detected, and although its radial intensity profile shows a tentative peak toward the central star, the signal shown on the zeroth-moment map is shifted from the disk location. Assuming LTE and using the CS excitation temperature derived toward the MWC 480 disk (see Section 3.3), we derived upper limits on the column densities that we compare with results from disk chemistry modeling in Figure 8, presented in Section 4.4.

4. Astrochemical Modeling

To further investigate the S chemistry in protoplanetary disks, we computed a grid of astrochemical models tuned to the MWC 480 disk, which is the disk in which we observed the most S-bearing molecules (see Section 2.2).

4.1. Protoplanetary Disk Physical Structure

Our fiducial protoplanetary disk astrochemical model is based on the MWC 480 disk model developed in Le Gal et al. (2019b). It consists of a 2D parametric physical structure in which the chemistry is postprocessed (see Section 4.2). We consider here a simplistic physical structure in the sense that the disk is assumed to be symmetric azimuthally and with respect to the midplane. Such a disk physical structure can thus be described in cylindrical coordinates centered on the star along two perpendicular axes characterizing the radius and height in the disk. Figure 4 shows the profiles of the gas temperature and density throughout the disk, for which the physical parameters used to compute the physical structure of MWC 480 are summarized in Table 3 and the parameterization is briefly summarized below, following Le Gal et al. (2019b).

For a given radius r from the central star, the vertical temperature profile is computed following the formalism developed by Dartois et al. (2003):

$$T(z) = \begin{cases} T_{\rm mid} + (T_{\rm atm} - T_{\rm mid})\left[\sin\left(\frac{\pi z}{2 z_q}\right)\right]^{2\delta} & \text{if } z < z_q \\ T_{\rm atm} & \text{if } z \geqslant z_q, \end{cases} \quad (7)$$

where $T_{\rm mid}$ and $T_{\rm atm}$ are, respectively, the midplane and atmosphere temperatures that vary as a power law of the radii (Beckwith et al. 1990; Piétu et al. 2007; Le Gal et al. 2019b). $z_q = 4H$, with H the pressure scale height, which, assuming vertical hydrostatic equilibrium, can be expressed as follows:

$$H = \sqrt{\frac{k_{\rm B}\, T_{\rm mid}\, r^3}{\mu\, m_{\rm H}\, G\, M_\star}}, \quad (8)$$

with $k_{\rm B}$ the Boltzmann constant, $\mu = 2.4$ the reduced mass of the gas, $m_{\rm H}$ the proton mass, G the gravitational constant, and $M_\star$ the mass of the central star. The midplane temperature $T_{\rm mid}$ is estimated following a simple irradiated passive flared disk approximation (e.g., Chiang & Goldreich 1997;

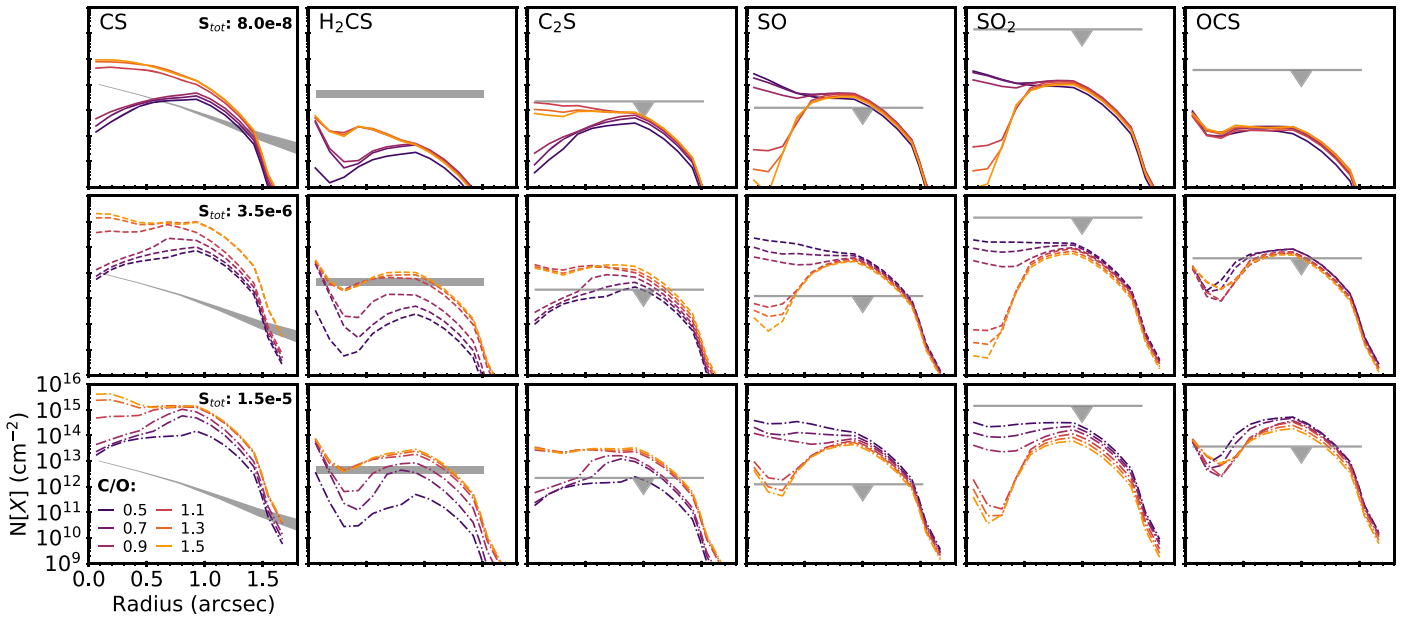

Figure 8. CS, H_2CS, C_2S, SO, SO_2, and OCS modeled column densities tuned to the MWC 480 disk, vertically integrated from the disk upper layer to the midplane and convolved to a resolution of 0.″5 to facilitate the comparison with the observations. The modeled column densities are shown by the solid lines investigating the impact of the C/O and S/H ratios. Observational error bars and upper limits derived toward the MWC 480 disk are indicated in gray. Note that the scales are replicated in all panels.

Table 3
Physical Parameters Used for Our Disk Models

Parameters	MWC 480[a]
Stellar mass: $M_\star$ ($M_\odot$)	1.8
Disk mass: M_d ($M_\odot$)	0.18
Characteristic radius: R_c (au)	100
Outer cutoff radius: R_{out} (au)	500
Density power-law index: γ	1.5
Midplane temperature at R_c[b]: T_{100au} (K)	30
Atmosphere temperature at R_c: T_{100au} (K)	48
Surface density at R_c: g cm^{-2}	5.7
Temperature power-law index: q	0.5
Vertical temperature gradient index: β	2
UV flux: f_{UV,R_c} (in units from Draine 1978)	8500[c]

Notes.
[a] These are the values used for the model developed in Le Gal et al. (2019b) and that we are using here to interpret the observations presented in the present work.
[b] The midplane temperature is estimated from Equation (9), the luminosity, and a typical flaring angle $\varphi = 0.05$.
[c] From Dutrey et al. (2011), originally computed from the Kurucz (1993) ATLAS9 of stellar spectra.

Dullemond et al. 2001):

$$T_{\rm mid}(r) \approx \left(\frac{\varphi L_\star}{8\pi r^2 \sigma_{\rm SB}}\right)^{1/4}, \quad (9)$$

with $L_\star = 21.9\,L_\odot$ the stellar luminosity (see Table 1), $\sigma_{\rm SB}$ the Stefan−Boltzmann constant, and $\varphi = 0.05$ a typical flaring angle value (e.g., Brauer et al. 2008; Baillié & Charnoz 2014). The atmosphere temperature, $T_{\rm atm}$, is based on observational constraints. So here we consider $T_{\rm atm} = T_{\rm atm,100\,au}\left(\frac{r}{100\,\rm au}\right)$, with $T_{\rm atm,100\,au} = 48$ K from Guilloteau et al. (2011).

The disk is assumed to be in hydrostatic equilibrium. Thus, for a given vertical temperature profile, the vertical density structure is determined by solving the equation of hydrostatic equilibrium, as described by Equations (17)−(20) in Le Gal et al. (2019b).

The surface density of the disk is assumed to follow a simple power law varying as $r^{-3/2}$ (Shakura & Sunyaev 1973; Hersant et al. 2009):

$$\Sigma(r) = \Sigma_{R_c}\left(\frac{r}{R_c}\right)^{-3/2}, \quad (10)$$

where Σ_{R_c} is the surface density at the characteristic radius that can be expressed as a function of the mass of the disk, $M_{\rm disk}$, and its outer radius, $R_{\rm out}$:

$$\Sigma_{R_c} = \frac{M_{\rm disk} R_c^{-3/2}}{4\pi\sqrt{R_{\rm out}}}, \quad (11)$$

with $M_{\rm disk} = 0.18\,M_\odot$ (Guilloteau et al. 2011).

The visual extinction profile is derived from the hydrostatic density profile using the gas-to-extinction ratio of $N_{\rm H}/A_{\rm V} = 1.6 \times 10^{21}$ (Wagenblast & Hartquist 1989), with $N_{\rm H} = N({\rm H}) + 2N(H_2)$ the vertical hydrogen column density of hydrogen nuclei. This gas-to-extinction ratio assumes a typical mean grain radius size of 0.1 μm and dust-to-mass ratio of 0.01. While the use of a grain-size distribution including both large and small grains would be more realistic, its impact on the chemistry remains poorly constrained and would require a dedicated study such as, e.g., the one recently performed in Gavino et al. (2021). We therefore opt for the simpler approximation, which should be sufficient to provide an interpretative framework for the presented observations.

Finally, to compute the UV flux profile, we multiplied the UV flux factor impinging on the disk with e^{-x}, where x contains the visual extinction profile. The unattenuated UV flux factor, $f_{\rm UV}$, at a given radius r depends both on the photons

coming directly from the central embedded star and on the photons that are downward-scattered by small grains in the upper atmosphere of the disk. Thus, following Wakelam et al. (2016), we consider

$$f_{\rm UV} = \frac{f_{{\rm UV},R_c}/2}{\left(\frac{r}{R_c}\right)^2 + \left(\frac{4{\rm H}}{R_c}\right)^2}. \quad (12)$$

4.2. Protoplanetary Disk Chemical Model

The disk chemistry is computed time-dependently in 1 + 1D based on the gas-grain astrochemical code Nautilus, which includes gas-phase, grain-surface, and grain-bulk chemistry (Wakelam et al. 2017; Le Gal et al. 2019b, 2019a). This rate-equation gas-grain chemical code follows the formalism described in Hasegawa et al. (1992) and Hasegawa & Herbst (1993). We used the same chemical network as Le Gal et al. (2019b), which is based on the KInetic Database for Astrochemistry (KIDA)[27] and includes recent updates (Fuente et al. 2017; Le Gal et al. 2017; Vidal et al. 2017; Le Gal et al. 2019b). It contains 589 gas-phase species and 540 solid-state species interacting together through a total of 13,402 reactions. Chemical exchanges in between the gas-phase, grain-surface, and grain-bulk phases are included, with adsorption and desorption processes linking the gas and surface phases, and swapping processes linking the mantle and surface of grains. Several desorption mechanisms are taken into account: thermal desorption (Hasegawa et al. 1992), cosmic-ray-induced desorption (Hasegawa & Herbst 1993), photodesorption, and chemical desorption (e.g., Le Gal et al. 2017, and references therein). In the gas phase typical bimolecular ion−neutral and neutral−neutral reactions are considered, as well as cosmic-ray-induced processes, photoionizations, and photodissociations caused by both stellar and interstellar UV photons.

First, we model the chemical evolution of a representative starless dense molecular cloud, with a characteristic age of 1 Myr (e.g., Elmegreen 2000; Hartmann et al. 2001) and typical constant physical conditions: grain and gas temperatures of 10 K, a total gas density of $2 \times 10^4\,{\rm cm}^{-3}$, $\zeta = 1 \times 10^{-17}\,{\rm s}^{-1}$ per H_2, and a visual extinction of 30 mag. For this first-stage model, we consider the initial chemical conditions to be close to diffuse gas conditions, i.e., all the elements are initially in atomic form (see Table 4) except hydrogen, which is assumed to be already fully molecular. The elements taken into account in our simulation with an ionization potential lower than that of hydrogen (13.6 eV) are thus assumed to be initially singly ionized; see Table 4. The outcoming chemical gas and ice compositions of this representative parent molecular cloud serve as the initial chemistry for our 1 + 1D disk model, for which the physical parameters are described in Le Gal et al. (2019b). Second, we run the chemistry of our 1 + 1D disk model up to 1 Myr, the typical chemical age of a disk when dust evolution is not included (e.g., Cleeves et al. 2015), which is the case for our disk model. While the disk chemistry has not reached steady state at that time, its evolution is slow enough that the results presented here hold for a disk twice as young or old.

[27] http://kida.obs.u-bordeaux1.fr/

Table 4
Initial Elemental Abundances

Species	$n_i/n_{\rm H}$	Reference
H_2	0.5	
He	9.0×10^{-2}	1
C^+	1.7×10^{-4}	2
N	6.2×10^{-5}	2
O	$3.4 \times 10^{-4} - 1.1 \times 10^{-4}$	3
S^+	$8.0 \times 10^{-8} - 1.5 \times 10^{-5}$	4
Si^+	8.0×10^{-9}	5
Fe^+	3.0×10^{-9}	5
Na^+	2.0×10^{-9}	5
Mg^+	7.0×10^{-9}	5
P^+	2.0×10^{-10}	5
Cl^+	1.0×10^{-9}	5
F^+	6.7×10^{-9}	6

References. (1) Wakelam & Herbst 2008; (2) Jenkins 2009; (3) we varied the oxygen elemental abundance in this range to test the impact of the C/O ratio (see Section 4.4); (4) we varied the sulfur elemental abundance in this range to test the impact of the S/H ratio (see Section 4.3); (5) Graedel et al. 1982; (6) Neufeld et al. 2015.

4.3. Impact of the S/H Ratio

In the context of S-bearing molecules, a crucial parameter to study is the S/H elemental ratio, i.e., the total amount of S not locked into refractory compounds and thus available for the volatile S chemistry. Figure 8 shows the modeled column densities of CS, H_2CS, SO, SO_2, C_2S, and OCS as a function of distance from the central star for a range of C/O ratios (further described in Section 4.4) and for three different elemental S/H ratios: the usual highly depleted S abundance value of 8.0×10^{-8}, corresponding to the "low metal" abundances from Graedel et al. (1982); an intermediate S abundance value of 3.5×10^{-6}, corresponding to the value derived in PDR regions (Goicoechea et al. 2006; Le Gal et al. 2019a); and the solar abundance (1.5×10^{-5}; Asplund et al. 2009). For comparison, estimated and upper limits of the column densities of the six S-bearing species we observed toward the MWC 480 disk are also displayed in Figure 8.

While for a low S elemental abundance, the column density of CS can be reproduced for C/O $\gtrsim$0.9, similarly to what has been found to reproduce the column densities of CH_3CN and HC_3N in the same disk (Le Gal et al. 2019a), the H_2CS column densities are underpredicted. On the contrary, no S depletion, i.e., considering that all the solar S abundance is available for S chemistry in disks, allows the reproduction of H_2CS but cannot reproduce the column density of CS, which is then overpredicted. Models without S depletion also require different C/O ratios to reproduce the column densities of C_2S and SO.

Since H_2CS is a more complex molecule as compared to CS, we suspect that its underproduction in our model is more likely to be due to missing formation pathways than differences in elemental abundances between models and observations. Experimental and theoretical chemical studies are needed to better constrain the formation pathways of H_2CS.

4.4. Impact of the C/O Ratio

The relative gas-phase abundances of the chemical elements are known to strongly influence the chemistry of star-forming regions (van Dishoeck & Blake 1998). At the onset of star formation, a substantial amount of the total budget of the main

Table 5
Observed versus Modeled Disk-integrated Column Densities (in cm^{-2}) and CS/SO Ratio in MWC 480 Out to 1.″5

	CS	H_2CS	C_2S	SO	SO_2	OCS	CS/SO[a]	CS/SO[b]
Observed Value	$6.6^{+0.5}_{-0.5} \times 10^{12}$	$4.0^{+2.1}_{-0.9} \times 10^{12}$	$\lesssim 2.2 \times 10^{12}$	$\lesssim 1.2 \times 10^{12}$	$\lesssim 1.4 \times 10^{15}$	$\lesssim 3.7 \times 10^{13}$	$\gtrsim 5.5$	
C/O = 0.5; S/H = 8×10^{-8}	1.1×10^{12}	8.1×10^{09}	1.1×10^{11}	5.3×10^{12}	9.6×10^{12}	1.4×10^{11}	0.21	0.71
C/O = 0.7	1.5×10^{12}	4.3×10^{10}	1.7×10^{11}	4.8×10^{12}	1.1×10^{13}	1.9×10^{11}	0.31	1.5
C/O = 0.9	1.8×10^{12}	4.9×10^{10}	2.1×10^{11}	3.1×10^{12}	8.2×10^{12}	1.5×10^{11}	0.58	3.2
C/O = 1.1	2.0×10^{13}	1.1×10^{11}	8.6×10^{11}	1.4×10^{12}	4.5×10^{12}	1.3×10^{11}	14	15
C/O = 1.3	3.3×10^{13}	1.1×10^{11}	6.1×10^{11}	1.3×10^{12}	3.9×10^{12}	1.7×10^{11}	25	
C/O = 1.5	3.5×10^{13}	1.2×10^{11}	5.4×10^{11}	1.1×10^{12}	3.4×10^{12}	1.9×10^{11}	31	
C/O = 0.5; S/H = 3.5×10^{-6}	2.6×10^{13}	9.1×10^{10}	9.0×10^{11}	7.9×10^{13}	1.1×10^{14}	3.1×10^{13}	0.33	0.92
C/O = 0.7	3.9×10^{13}	2.0×10^{12}	1.5×10^{12}	3.9×10^{13}	6.4×10^{13}	3.0×10^{13}	1.0	1.1
C/O = 0.9	7.7×10^{13}	2.7×10^{12}	3.0×10^{12}	2.1×10^{13}	3.5×10^{13}	1.9×10^{13}	3.7	1.4
C/O = 1.1	3.1×10^{14}	5.3×10^{12}	1.0×10^{13}	1.0×10^{13}	2.5×10^{13}	2.2×10^{13}	31	11
C/O = 1.3	7.0×10^{14}	6.0×10^{12}	9.6×10^{12}	9.0×10^{12}	2.0×10^{13}	2.0×10^{13}	78	
C/O = 1.5	8.2×10^{14}	6.8×10^{12}	1.1×10^{13}	8.1×10^{12}	1.6×10^{13}	1.8×10^{13}	101	
C/O = 0.5; S/H = 1.5×10^{-5}; C/O = 0.5	5.8×10^{13}	4.2×10^{11}	9.2×10^{11}	1.7×10^{14}	2.0×10^{14}	1.8×10^{14}	0.34	
C/O = 0.7	1.7×10^{14}	5.3×10^{12}	3.3×10^{12}	8.3×10^{13}	1.0×10^{14}	1.5×10^{14}	2.0	
C/O = 0.9	3.0×10^{14}	7.8×10^{12}	5.3×10^{12}	4.9×10^{13}	5.5×10^{13}	1.0×10^{14}	6.1	
C/O = 1.1	6.2×10^{14}	1.3×10^{13}	1.7×10^{13}	1.8×10^{13}	3.2×10^{13}	9.7×10^{13}	34	
C/O = 1.3	1.1×10^{15}	1.5×10^{13}	1.9×10^{13}	1.6×10^{13}	2.3×10^{13}	7.7×10^{13}	69	
C/O = 1.5	1.5×10^{15}	1.6×10^{13}	2.0×10^{13}	1.4×10^{13}	1.7×10^{13}	6.1×10^{13}	107	

Notes.
[a] Models without dust settling.
[b] Models with dust settling (see Section 4.5).

chemical elements, such as oxygen (O) and carbon (C), is locked in refractory materials. Furthermore, for some of them, huge uncertainties remain on the nature and the form of a substantial part of their reservoir. This is in particular the case for oxygen, where ∼40% of the O budget remains unaccounted for (Whittet 2010; Jones & Ysard 2019; Öberg & Bergin 2021), which results in a nonnegligible uncertainty on the C/O ratio in the gas phase.

In order to mimic the differential depletion of volatiles, we varied the C/O ratio from 0.5 to 1.5 (see Table 4). The impact of the gas-phase C/O ratio on the column densities of CS, H_2CS, SO, SO_2, C_2S, and OCS is shown in Figure 8 and summarized in Table 5. As can be expected, for the carbonated sulfur molecules, i.e., the S-bearing species containing a C–S bond, an O-poor chemistry (i.e., a high C/O ratio) results in higher column densities, while the reverse is seen for the oxygenated sulfur molecules (i.e., the molecules containing an O–S bond). This behavior is most prominent in the inner 1.″0 (i.e., ∼160 au) of the disk for most molecules. Interestingly, the best model to fit the CS data is the most depleted S/H model.

The MAPS observations provide upper limits on SO, which allows us to calculate lower limits on the CS/SO ratio to which we can compare our model. Figure 9 shows how the modeled radial profile of the CS/SO column density ratio varies as a function of the elemental C/O ratio and total amount of sulfur. We only consider the two depleted S abundance models, since we ruled out models with solar S in Section 4.3, based on comparisons between observed and modeled CS radial profiles. We find that the CS/SO ratio is highly sensitive to the C/O ratio; a change in C/O from 0.5 to 1.5 increases the CS/SO ratio by up to 4 orders of magnitude. This is consistent with previous disk modeling results from Semenov et al. (2018), as well as with cloud chemistry predictions (e.g., Bergin et al. 1997; Nilsson et al. 2000). We can compare these model results with our observational lower limit of >5.5 (see Table 5). Based on the visual comparison between models and data in Figure 9, the C/O ratio needs to be ≳0.9 in order to reproduce the CS/SO ratio observation in the MWC 480 disk. We also provide disk-integrated CS/SO ratios for the relevant disk models in Table 5, and these confirm that only models with C/O > 0.9 are consistent with observations.

4.5. Impact of Dust Evolution

Dust evolution and in particular dust settling can have a profound effect on disk chemistry, including on the ratios of molecules that have been proposed as tracers of C/O. Wakelam et al. (2019) recently explored the impact of several disk parameters on the vertically integrated column densities of a set

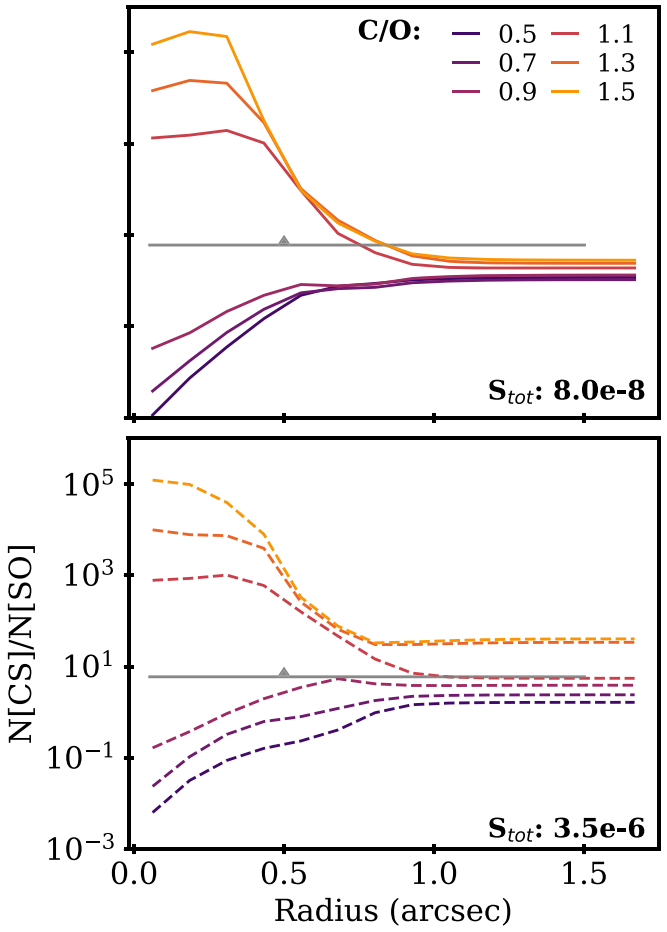

Figure 9. Calculated N(CS)/N(SO) column density ratios for a grid of models tuned to the MWC 480 disk investigating the impact of C/O and S/H ratios. Observations toward the MWC 480 disk are indicated by the gray horizontal lower limits. Because SO is not detected, the spatial distribution of SO in the disk is unknown. Thus, we extracted the upper limit on the SO emission for the exact same region of the disk area in which the CS emission is detected (see Section 3.7).

of molecules observed in the DM Tau disk. They found that dust settling can have a strong impact on the disk chemistry and can, in particular, enhance the chemical abundances of several carbon-bearing molecules such as CH_3CN and HC_3N. To test whether dust settling could change our conclusions on the C/O ratio in the MWC 480 disk, we ran an additional set of models, for a smaller grid of C/O values (from 0.5 to 1.1) and including similar dust settling to the fiducial one proposed in Wakelam et al. (2019) (i.e., their E2 model, where the settling occurs at $z/h = 1$). The results are depicted in Figure 10.

Comparing Figures 9 and 10, we see that dust settling indeed influences the variation of CS/SO ratio as a function of C/O ratio. With dust settling, the models with varying C/O produce column density ratios within 1 order of magnitude for radius $\gtrsim$0.″3. Without dust settling, at least for the inner disk (i.e., radius <0.″5), the models show a spread of 4–8 orders of magnitude. Therefore, it seems that if dust settling is present in a disk, one can only derive whether C/O is smaller or larger than 1. Furthermore, one can note that for the outer disk (>0.″7) the models with varying C/O are almost indistinguishable when dust settling is present (in particular for the most depleted S/H model).

5. Discussion

5.1. Is the CS/SO Column Density Ratio a Good C/O Ratio Proxy?

As shown in Figure 9, our modeling results suggest that the CS/SO column density ratio is a promising probe of the C/O ratio in disks (see Section 4.4). We find that an elevated C/O ratio (i.e., a supersolar C/O) is required for the MWC 480 disk in order to reproduce the observed CS/SO ratio. A C/O ratio $\gtrsim$0.9 seems reasonable for the MWC 480 chemistry, as it results in both a detectable column density of the S organic compounds H_2CS and a good match to the observed column densities of nitriles (Le Gal et al. 2019a). Moreover, while dust settling seems to impact the CS/SO ratio with varying C/O, we are still finding results converging toward a supersolar C/O. It is worth noticing that this is in very good agreement with the results found from other molecules probed within the MAPS program, i.e., CO isotopologues and C_2H. Using an independent disk model, we found that a supersolar C/O is also required to reproduce the CO isotopologues and C_2H observations in the same disk (Bosman et al. 2021; Alarcón et al. 2021). Furthermore, we also checked the predicted water vapor abundances from our models, and in the elevated C/O case they are consistent with the upper limits provided by the WISH project (van Dishoeck et al. 2021), while water is overpredicted in the low C/O models. Thus, (1) there seems to be a robust convergence toward an elevated C/O ratio and (2) the CS/SO ratio appears to be an additional and independent good probe of the C/O ratio.

In Figure 11, we show the lower limits found for the N(CS)/N(SO) column density ratio derived in each of the protoplanetary disks observed with MAPS. Among this sample, the ratio varies by a factor ∼10, which leads to similar C/O ratio constraints for each of the disks, i.e., a supersolar C/O if we consider that our disk model results hold for the other four MAPS disks. However, these preliminary results would need to be corroborated by deeper upper limits on SO and further modeling investigations that would be addressed in forthcoming studies. Additional CS/SO measurements toward a larger sample of protoplanetary disks would also be a good way to measure how common is the C/O ratio expected to be elevated in disks.

5.2. Interpretation of Disk S/H Ratio

In protoplanetary disks, the S/H elemental ratio has been much less studied, and therefore less well constrained, than the C/O and C/H ratios. As of today, we still do not know what the major S reservoir(s) in disks is (are) and in which form it resides (solid or gaseous). However, this is an important parameter to constrain as well, not only to solve the current disk modeling tension found to interpret the high H_2CS/CS ratio in MWC 480 but also because, more generally, many S-bearing species are observed in comets and do play an important role in the building up of prebiotic molecules and in planet habitability.

Recently, based on the abundances of B star photospheres, Kama et al. (2019) found that ∼81%–97% of the S budget should be locked in disk refractory material. Following the findings of Keller et al. (2002), the former authors proposed that most of the sulfur should be locked in the form of solid FeS in disks, rather than in polymeric S_n ($n = 2$–8) molecules, where the latter has been proposed for decades as a potential

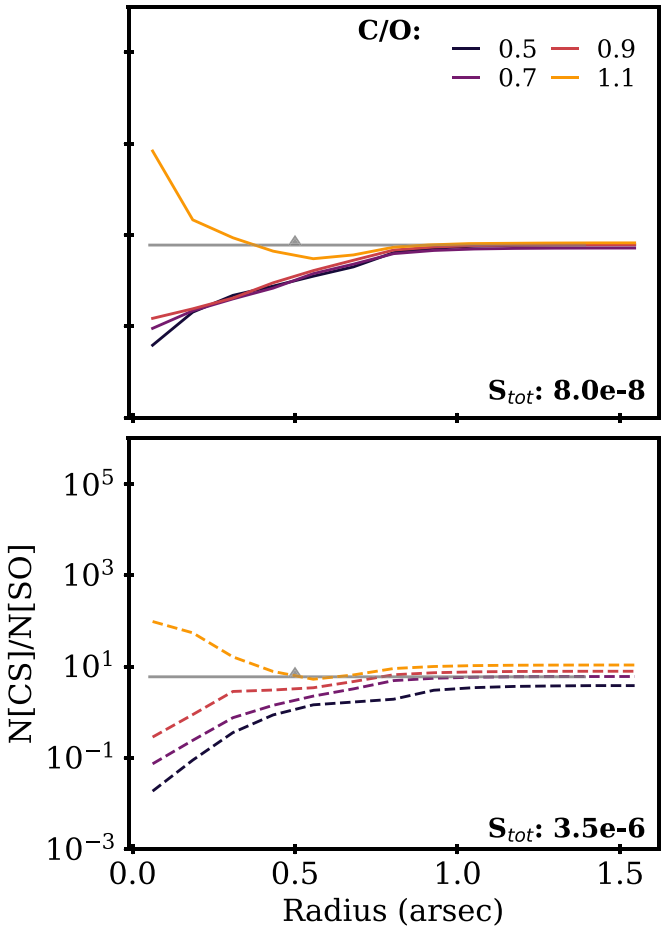

Figure 10. Same as Figure 9, but with models considering dust settling as described in Section 4.5.

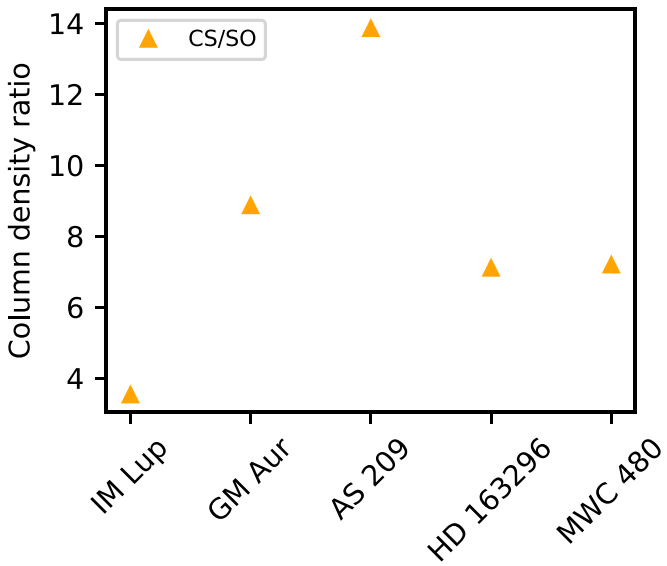

Figure 11. Lower limits on the N(CS)/N(SO) column density ratio derived from the MAPS observations.

hidden S reservoir in the ISM (e.g., Wakelam et al. 2004). However, the observations of solid FeS have not yet been confirmed in disks (Keller et al. 2002), whereas hints of solid S_n were recently reported on the comet 67P/C-G with the detections of S_2, S_3, and S_4 from the Rosetta mission (Calmonte et al. 2016), although these detections constitute only ∼0.2% of the total detected S content of 67P/C-G.

The comparison with comets' sulfur-bearing molecule content is, however, instructive. In particular, it is interesting to note that in the inventory of the molecular abundances detected in comets compiled by Bockelée-Morvan & Biver (2017) an H_2CS/CS ratio of ≈0.45 is reported, i.e., close to the value we measured in the MWC 480 protoplanetary disk (see Section 3.4 and Le Gal et al. 2019b). Another relevant point stressed in the Bockelée-Morvan & Biver (2017) review is that one of the most abundant S-bearing molecules detected in comets is OCS, which could be another potential S reservoir. OCS is indeed the only S-bearing molecule unambiguously detected in ice mantles so far (Geballe et al. 1985; Palumbo et al. 1995). Furthermore, astrochemical shock modeling benchmarked to protostellar shock observations predicted that ≳50% of the sulfur ice reservoir resides in OCS (Podio et al. 2014; Holdship et al. 2016). The latter is therefore a promising S reservoir to interpret the high H_2CS/CS ratio we observed toward MWC 480 that is not reproducible with our model (see Section 4).

5.3. Could the Sulfur Organic Chemistry Be Underappreciated in Models?

In our model, and as previously described in Le Gal et al. (2019b), H_2CS is mainly formed from the following neutral–neutral and electronic dissociative recombination gas-phase reactions:

$$S + CH_3 \rightarrow H_2CS + H, \quad (13)$$

$$H_3CS^+ + e^- \rightarrow H_2CS + H, \quad (14)$$

with H_3CS^+ originating from the $S^+ + CH_4$ reaction.

It is also formed, for a smaller contribution, from gas-grain chemistry where H_2CS is produced from successive hydrogenation on icy dust mantles and released for ∼1% in the gas phase by chemical reactive desorption. However, in our current model, there is no consideration of OCS grain-surface processing that could lead to the formation of S organics such as H_2CS and thus maybe help in better reproducing the observations. Because H_2CS is a more complex species compared to CS, we suspect that its underproduction is more likely due to missing formation pathways than an undepleted S gas-phase reservoir. The latter is inconsistent with CS observations (see Section 4.3). Laboratory experiments and theoretical chemical calculations for such mechanisms are required to further test our hypothesis. While the S reservoir could be changing from the inner to the outer disk regions, dedicated disk resolved S observations are also needed to further investigate the nature and identity of the S reservoir in disks, and how and if there is any chemical inheritance from molecular cloud stage to the planet-forming environment.

5.4. CS Disk Emission Asymmetries

In Section 3.1, we highlight asymmetries in the CS 2 − 1 emission spatial distribution toward four of the five targeted disks. Intriguingly, these asymmetries are not observed in the other molecular lines targeted within MAPS or in higher CS transitions (i.e., the 5 − 4 and 6 − 5 transitions published in Le Gal et al. 2019b). We also do not see any such asymmetries in the dust emission of any of the targeted disks. So these asymmetries appear to be different than, for instance, the one

detected in CS $J = 7 - 6$ toward the HD 142527 disk (van der Plas et al. 2014). However, we should note that in the present study we are reporting CS $2 - 1$ asymmetries that are likely emitting from disk layers closer to the midplane than the CS $7 - 6$ would. Toward the GM Aur, AS 209, and HD 163296 disks, the CS $2 - 1$ emission asymmetries seem to correlate with their respective disk inclination, i.e., the CS $2 - 1$ emission is brightest in the near side of the disk (see Figure 2). However, toward MWC 480, we observe the reverse: the CS $2 - 1$ emission is brightest in the far side of the disk. Here we investigate what could cause such asymmetries.

The HD 163296 disk is known to harbor both a jet (Grady et al. 2000) and a disk wind. The latter was discovered through ^{12}CO observations by Klaassen et al. (2013) and is also further characterized using CO isotopologue observations as a part of MAPS (Booth et al. 2021). According to the geometry of jet, wind, and viewing angle proposed in Ellerbroek et al. (2014), the far side of the disk is supposed to be viewed through the disk's wind and jet, which is also the disk side where we found the CS $2 - 1$ emission to be the weakest. Thus, a speculative interpretation could be that the disk's wind and jet impact the CS content, or simply the emission of the $2 - 1$ line, and could therefore explain the decline in CS $2 - 1$ flux in the side of the disk affected by the wind and jet. For instance, if the wind impacts the local C/O ratio, it thus could impact the local disk chemistry and maybe the total amount of the CS bulk lying closer to the midplane layer; or/and if the wind is also made of dust, the line emission below the wind with respect to the observer could be hampered owing to dust wind opacity. However, follow-up observations of CS toward both the HD 163296 disk and wind would be required to test this hypothesis.

Similarly, MWC 480 is known to be driving a bipolar jet aligned with the disk semiminor axis (Grady et al. 2010). Notably, the jet flow appears denser in the SW direction, which could explain the decrease in CS $2 - 1$ emission we observe in the same direction. A better characterization of this jet is required to assess how it could impact the CS $2 - 1$ disk emission.

Hints for a disk wind are also found toward the AS 209 disk (e.g., Fang et al. 2018; Banzatti et al. 2019, and references therein), but, to our knowledge, the orientation and spatial distribution of the latter remain to be determined. Another point to mention about the AS 209 disk is that its west half side is known to be cloud contaminated (Öberg et al. 2011; Huang et al. 2016; Teague et al. 2018a). While it strongly impacts the ^{12}CO $2 - 1$ and HCO^+ $1 - 0$ line emission in this disk (see Figures 3 and 5 in Law et al. 2021), this cloud contamination does not match with the CS $2 - 1$ asymmetries we are finding in the present work.

As for GM Aur, Macías et al. (2018) discuss the possibility of a radio jet. Furthermore, the GM Aur disk is also the only transitional disk of our sample—i.e., the only one with a central dust cavity—and, as characterized by its complex gas structures, it is known to be affected by much more prominent gas dynamics than the other disks of our sample (e.g., Huang et al. 2021, and references therein). Therefore, the CS $2 - 1$ asymmetry of this disk is probably the least difficult to justify but would require further observations to be linked with the other gas kinematics features observed in this disk.

While all these hypotheses seem appealing, further investigations are required to truly determine the nature of these CS $2 - 1$ asymmetries and in particular to identify whether they are tracing one specific characteristic of disk evolution or whether they could be explained by multiple phenomena.

6. Conclusion

We presented ALMA observations of S-bearing molecules observed toward the five protoplanetary disks targeted by the MAPS ALMA Large Program, orbiting the IM Lup, GM Aur, and AS 209 T Tauri stars and the two Herbig Ae stars HD 163296 and MWC 480.

Our main findings are summarized below:

1. The CS $2 - 1$ line was observed within MAPS and detected toward all five disks, displaying a variety of radial intensity profiles and spatial distributions across the sample, including intriguing apparent azimuthal asymmetries.
2. Using complementary ALMA observations of CS $5 - 4$ and $6 - 5$ in one of the disks, i.e., the MWC 480 disk, allows us to assess the CS column density across the full sample, assuming a temperature in the range 10–30 K, which results in $N_{\rm tot}({\rm CS}) \approx (0.2 - 5) \times 10^{13}\,{\rm cm}^{-2}$.
3. C_2S and SO lines were also covered within MAPS. While no detection can be robustly claimed from these observations, we provide upper limits on their column densities, with upper limits in the range $10^{12} - 10^{13}\,{\rm cm}^{-3}$ for C_2S and $(1 - 5) \times 10^{12}\,{\rm cm}^{-3}$ for SO. In particular, we used the upper limit on SO to derive lower limits on the CS/SO ratio across the MAPS sample, which is found to range from $\sim$4 to 14.
4. Using complementary ALMA programs, we find $N(H_2CS)/N(CS) \approx 2/3$ in MWC 480. This high ratio suggests that substantial S reservoirs in disks may be in the form of S organics (i.e., $C_xH_yS_z$).
5. Using astrochemical disk models, we find that the CS/SO ratio is a promising probe for the elemental C/O ratio. CS/SO varies by more than 4 orders of magnitude when C/O varies from 0.5 to 1.5.
6. For MWC 480, without considering dust settling, we find C/O $\gtrsim$ 0.9, consistent with constraints from nitrile observations (Le Gal et al. 2019a). When considering dust settling, one can only derive whether C/O is smaller or larger than 1, but this remains consistent with a high C/O ratio under the specific conditions assumed in the modeling. More interestingly, this is confirmed with independent disk chemistry models predicting supersolar C/O based on the CO and C_2H MAPS data (Bosman et al. 2021).
7. We find a depleted gas-phase S/H ratio, suggesting either that part of the sulfur reservoir is locked in solid phase or that it remains in an unidentified gas-phase reservoir. More sulfur observations are required to confirm this and, to a larger extent, to identify the nature of the S reservoir (s).

Together these results illustrate the importance of sulfur chemistry in protoplanetary disks, demonstrating not only that sulfur-bearing molecule observations in such disks can serve to constrain the sulfur chemistry itself and its reservoir(s) but also that sulfur-bearing molecules are powerful tools to constrain other fundamental parameters, such as the elemental C/O ratio. Furthermore, sulfur-bearing molecules seem to uniquely

probe disk gas substructures, but this requires deeper observations to be further investigated and confirmed. Therefore, to fully comprehend the role of sulfur in disks, further theoretical and observational studies on the sulfur chemistry in disks are still required.

R.L.G. acknowledges support from CNES fellowship grant. K.I.Ö. acknowledges support from a Simons Foundation award (SCOL No. 321183, KO) and an NSF AAG grant (No. 1907653). R.T. acknowledges support from the Smithsonian Institution as a Submillimeter Array (SMA) Fellow. Y.A. acknowledges support by NAOJ ALMA Scientific Research grant code 2019-13B and Grant-in-Aid for Scientific Research 18H05222 and 20H05847. E.A.B. and A.D.B. acknowledge support from NSF AAG grant No. 1907653. F.M. acknowledges support from ANR of France under contract ANR-16-CE31-0013 (Planet-Forming-Disks) and ANR-15-IDEX-02 (through CDP "Origins of Life"). S.M.A. and J.H. acknowledge funding support from the National Aeronautics and Space Administration under grant No. 17-XRP17 2-0012 issued through the Exoplanets Research Program. J.H. acknowledges support for this work provided by NASA through the NASA Hubble Fellowship grant No. HST-HF2-51460.001-A awarded by the Space Telescope Science Institute, which is operated by the Association of Universities for Research in Astronomy, Inc., for NASA, under contract NAS5-26555. I.C. was supported by NASA through the NASA Hubble Fellowship grant HST-HF2-51405.001-A awarded by the Space Telescope Science Institute, which is operated by the Association of Universities for Research in Astronomy, Inc., for NASA, under contract NAS5-26555. V.V.G. acknowledges support from FONDECYT Iniciación 11180904 and ANID project Basal AFB-170002. C.J.L. acknowledges funding from the National Science Foundation Graduate Research Fellowship under grant DGE1745303. J.B.B. acknowledges support from NASA through the NASA Hubble Fellowship grant No. HST-HF2-51429.001-A, awarded by the Space Telescope Science Institute, which is operated by the Association of Universities for Research in Astronomy, Inc., for NASA, under contract NAS5-26555. K.R.S. acknowledges the support of NASA through Hubble Fellowship Program grant HST-HF2-51419.001, awarded by the Space Telescope Science Institute, which is operated by the Association of Universities for Research in Astronomy, Inc., for NASA, under contract NAS5-26555. C.W. acknowledges financial support from the University of Leeds, STFC, and UKRI (grant Nos. ST/R000549/1, ST/T000287/1, MR/T040726/1). J.D.I. acknowledges support from the Science and Technology Facilities Council of the United Kingdom (STFC) under ST/T000287/1. L.I.C. gratefully acknowledges support from the David and Lucile Packard Foundation and Johnson & Johnson's WiSTEM2D Program. H.N. acknowledges support from NAOJ ALMA Scientific Research grant code 2018-10B and Grant-in-Aid for Scientific Research 18H05441. T.T. is supported by JSPS KAKENHI grant Nos. JP17K14244 and JP20K04017. Y.Y. is supported by IGPEES, WINGS Program, the University of Tokyo. K.Z. acknowledges the support of the Office of the Vice Chancellor for Research and Graduate Education at the University of Wisconsin–Madison with funding from the Wisconsin Alumni Research Foundation, and the support of NASA through Hubble Fellowship grant No. HST-HF2-51401.001.

Facility: ALMA .

Software: `CASA` (McMullin et al. 2007), `Astropy` (Astropy Collaboration et al. 2013), `Matplotlib` (Hunter 2007), `NumPy` (van der Walt et al. 2011), `emcee` (Foreman-Mackey et al. 2013), `SciPy` (Jones et al. 2001), `scikitimage` (van der Walt et al. 2014), `Gofish` (Teague 2019), `VISIBLE` (Loomis et al. 2018b).

Appendix
Imaging of SO, C_2S, OCS, and SO_2

In this appendix we present the zeroth-moment map, radially deprojected and azimuthally averaged intensity profile, and shifted and stacked disk-integrated spectrum zeroth-moment maps and radial intensity profiles for the strongest C_2S and SO lines serendipitously covered by MAPS (Figure A1) and for the SO_2 and OCS lines covered in our complementary Cycle 6 ALMA data (Figure A2). All of them are derived for the same emitting area as the detected CS $2-1$ transition (see Table 2).

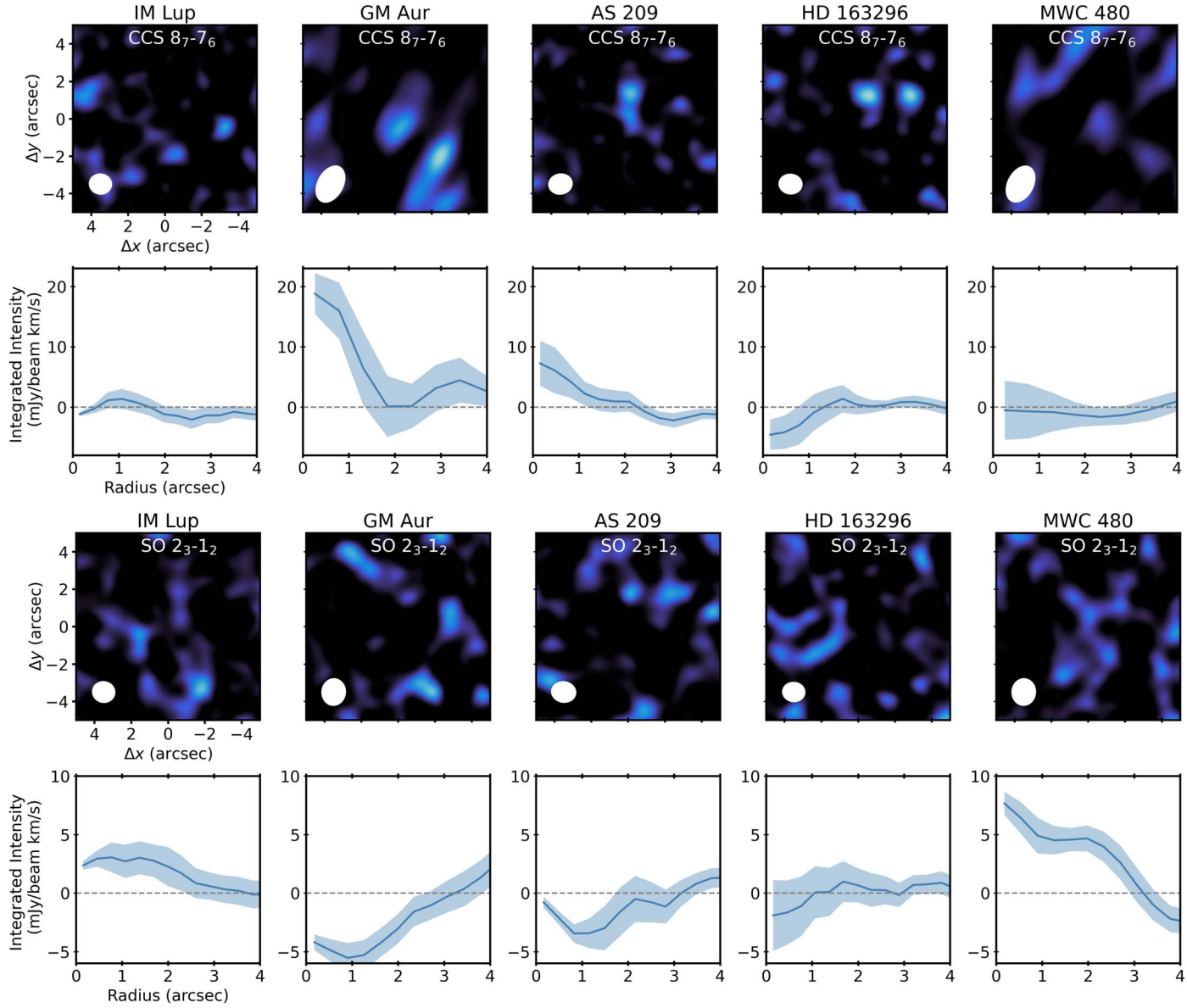

Figure A1. First and third rows: zeroth-moment maps of C_2S $8_7 - 7_6$ (first row) and SO $2_3 - 1_2$ (third row). Synthesized beams are shown in the lower left corner of each panel. Second and fourth rows: radially deprojected and azimuthally averaged intensity profiles of the C_2S $8_7 - 7_6$ (second row) and SO $2_3 - 1_2$ (fourth row) emission lines.

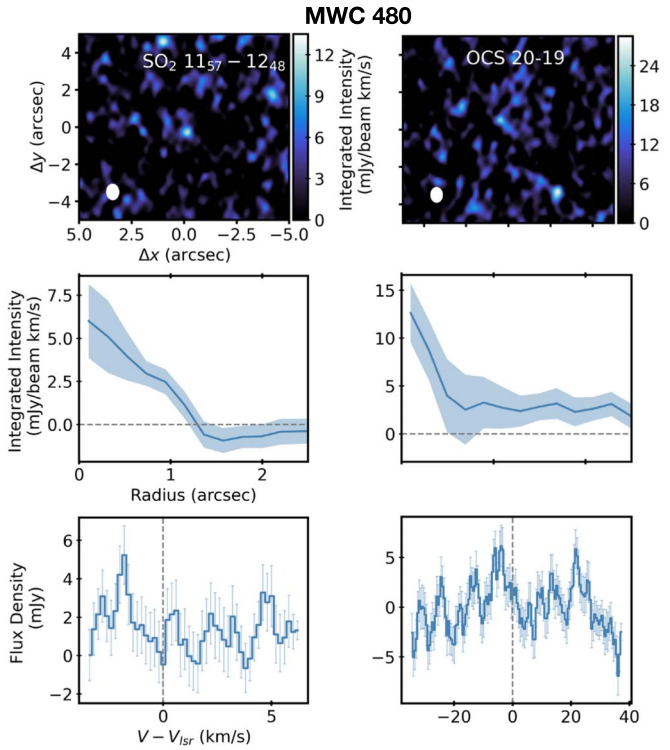

Figure A2. Zeroth-moment map (top panels), radially deprojected and azimuthally averaged intensity profiles within 1σ, similar to Figures 1 and 3 (middle panels), and shifted and stacked disk-integrated line spectra within 1σ (bottom panels). These last uncertainties are calculated on a per-channel basis, taking into account decorrelation along the spectral axis (see also Yen et al. 2016; Ilee et al. 2021).

ORCID iDs

Romane Le Gal https://orcid.org/0000-0003-1837-3772
Karin I. Öberg https://orcid.org/0000-0001-8798-1347
Richard Teague https://orcid.org/0000-0003-1534-5186
Ryan A. Loomis https://orcid.org/0000-0002-8932-1219
Charles J. Law https://orcid.org/0000-0003-1413-1776
Catherine Walsh https://orcid.org/0000-0001-6078-786X
Edwin A. Bergin https://orcid.org/0000-0003-4179-6394
François Ménard https://orcid.org/0000-0002-1637-7393
David J. Wilner https://orcid.org/0000-0003-1526-7587
Sean M. Andrews https://orcid.org/0000-0003-2253-2270
Yuri Aikawa https://orcid.org/0000-0003-3283-6884
Alice S. Booth https://orcid.org/0000-0003-2014-2121
Gianni Cataldi https://orcid.org/0000-0002-2700-9676
Jennifer B. Bergner https://orcid.org/0000-0002-8716-0482
Arthur D. Bosman https://orcid.org/0000-0003-4001-3589
L. Ilse Cleeves https://orcid.org/0000-0003-2076-8001
Ian Czekala https://orcid.org/0000-0002-1483-8811
Kenji Furuya https://orcid.org/0000-0002-2026-8157
Viviana V. Guzmán https://orcid.org/0000-0003-4784-3040
Jane Huang https://orcid.org/0000-0001-6947-6072
John D. Ilee https://orcid.org/0000-0003-1008-1142
Hideko Nomura https://orcid.org/0000-0002-7058-7682
Chunhua Qi https://orcid.org/0000-0001-8642-1786
Kamber R. Schwarz https://orcid.org/0000-0002-6429-9457
Takashi Tsukagoshi https://orcid.org/0000-0002-6034-2892
Yoshihide Yamato https://orcid.org/0000-0003-4099-6941
Ke Zhang https://orcid.org/0000-0002-0661-7517

References

Aikawa, Y., van Zadelhoff, G. J., van Dishoeck, E. F., & Herbst, E. 2002, A&A, 386, 622
Alarcón, F., Bosman, A. D., Bergin, E. A., et al. 2021, ApJS, 257, 8
Alcalá, J. M., Manara, C. F., Natta, A., et al. 2017, A&A, 600, A20
Andrews, S. M., Huang, J., Pérez, L. M., et al. 2018, ApJ, 869, L41
Asplund, M., Grevesse, N., Sauval, A. J., & Scott, P. 2009, ARA&A, 47, 481
Astropy Collaboration, Robitaille, T. P., Tollerud, E. J., et al. 2013, A&A, 558, A33
Baillié, K., & Charnoz, S. 2014, ApJ, 786, 35
Banzatti, A., Pascucci, I., Edwards, S., et al. 2019, ApJ, 870, 76
Beck, T. L., & Bary, J. S. 2019, ApJ, 884, 159
Beckwith, S. V. W., Sargent, A. I., Chini, R. S., & Guesten, R. 1990, AJ, 99, 924
Bergin, E. A., Aikawa, Y., Blake, G. A., & van Dishoeck, E. F. 2007, in Protostars and Planets V, ed. B. Reipurth, D. Jewitt, & K. Keil (Tucson, AZ: Univ. Arizona Press), 751
Bergin, E. A., Goldsmith, P. F., Snell, R. L., & Langer, W. D. 1997, ApJ, 482, 285
Bergner, J. B., Guzmán, V. G., Öberg, K. I., Loomis, R. A., & Pegues, J. 2018, ApJ, 857, 69
Bergner, J. B., Öberg, K. I., Bergin, E. A., et al. 2019, ApJ, 876, 25
Bisschop, S. E., Jørgensen, J. K., Bourke, T. L., Bottinelli, S., & van Dishoeck, E. F. 2008, A&A, 488, 959
Biver, N., Moreno, R., Bockelée-Morvan, D., et al. 2016, A&A, 589, A78
Bockelée-Morvan, D., & Biver, N. 2017, RSPTA, 375, 20160252
Bockelée-Morvan, D., Crovisier, J., Mumma, M. J., & Weaver, H. A. 2004, in Comets II, ed. M. C. Festou, H. U. Keller, & H. A. Weaver (Tucson, AZ: Univ. Arizona Press), 391
Boogert, A. C. A., Gerakines, P. A., & Whittet, D. C. B. 2015, ARA&A, 53, 541
Booth, A. S., Tabone, B., Ilee, J. D., et al. 2021, ApJS, 257, 16
Booth, A. S., van der Marel, N., Leemker, M., van Dishoeck, E. F., & Ohashi, S. 2021, A&A, 651, L6
Booth, A. S., Walsh, C., Kama, M., et al. 2018, A&A, 611, A16
Bosman, A. D., Alarcón, F., Bergin, E. A., et al. 2021, ApJS, 257, 7
Brauer, F., Dullemond, C. P., & Henning, T. 2008, A&A, 480, 859
Calmonte, U., Altwegg, K., Balsiger, H., et al. 2016, MNRAS, 462, S253
Chen, Y. J., Juang, K. J., Nuevo, M., et al. 2015, ApJ, 798, 80
Chiang, E. I., & Goldreich, P. 1997, ApJ, 490, 368
Cleeves, L. I., Bergin, E. A., Qi, C., Adams, F. C., & Öberg, K. I. 2015, ApJ, 799, 204
Cleeves, L. I., Öberg, K. I., Wilner, D. J., et al. 2018, ApJ, 865, 155
Czekala, I., Loomis, R. A., Teague, R., et al. 2021, ApJS, 257, 2
Dartois, E., Dutrey, A., & Guilloteau, S. 2003, A&A, 399, 773
Draine, B. T. 1978, ApJS, 36, 595
Drozdovskaya, M. N., van Dishoeck, E. F., Jørgensen, J. K., et al. 2018, MNRAS, 476, 4949
Dullemond, C. P., Dominik, C., & Natta, A. 2001, ApJ, 560, 957
Dutrey, A., Guilloteau, S., & Guelin, M. 1997, A&A, 317, L55
Dutrey, A., Semenov, D., Chapillon, E., et al. 2014, in Protostars and Planets VI, ed. H. Beuther et al. (Tucson, AZ: Univ. Arizona Press), 317
Dutrey, A., Wakelam, V., Boehler, Y., et al. 2011, A&A, 535, A104
Ellerbroek, L. E., Podio, L., Dougados, C., et al. 2014, A&A, 563, A87
Elmegreen, B. G. 2000, ApJ, 530, 277
Espaillat, C., D'Alessio, P., Hernández, J., et al. 2010, ApJ, 717, 441
Fairlamb, J. R., Oudmaijer, R. D., Mendigutía, I., Ilee, J. D., & van den Ancker, M. E. 2015, MNRAS, 453, 976
Fang, M., Pascucci, I., Edwards, S., et al. 2018, ApJ, 868, 28
Foreman-Mackey, D., Hogg, D. W., Lang, D., & Goodman, J. 2013, PASP, 125, 306
Franz, H. B., King, P. L., & Gaillard, F. 2019, in Volatiles in the Martian Crust, ed. J. Filiberto & S. P. Schwenzer (Amsterdam: Elsevier), 119
Fuente, A., Cernicharo, J., Agúndez, M., et al. 2010, A&A, 524, A19
Fuente, A., Goicoechea, J. R., Pety, J., et al. 2017, ApJL, 851, L49
Gaia Collaboration, Brown, A. G. A., Vallenari, A., et al. 2018, A&A, 616, A1
Gavino, S., Dutrey, A., Wakelam, V., et al. 2021, arXiv:2106.05888
Geballe, T. R., Baas, F., Greenberg, J. M., & Schutte, W. 1985, A&A, 146, L6
Goicoechea, J. R., Pety, J., Gerin, M., et al. 2006, A&A, 456, 565
Goldsmith, P. F., & Langer, W. D. 1999, ApJ, 517, 209
Goodman, J., & Weare, J. 2010, CAMCS, 5, 65
Grady, C. A., Devine, D., Woodgate, B., et al. 2000, ApJ, 544, 895
Grady, C. A., Hamaguchi, K., Schneider, G., et al. 2010, ApJ, 719, 1565
Graedel, T. E., Langer, W. D., & Frerking, M. A. 1982, ApJS, 48, 321
Guilloteau, S., Di Folco, E., Dutrey, A., et al. 2013, A&A, 549, A92

Guilloteau, S., Dutrey, A., Piétu, V., & Boehler, Y. 2011, A&A, 529, A105
Guilloteau, S., Reboussin, L., Dutrey, A., et al. 2016, A&A, 592, A124
Hartmann, L., Ballesteros-Paredes, J., & Bergin, E. A. 2001, ApJ, 562, 852
Hasegawa, T. I., & Herbst, E. 1993, MNRAS, 263, 589
Hasegawa, T. I., Herbst, E., & Leung, C. M. 1992, ApJS, 82, 167
Hersant, F., Wakelam, V., Dutrey, A., Guilloteau, S., & Herbst, E. 2009, A&A, 493, L49
Hirschmann, M. M. 2016, AmMin, 101, 540
Högbom, J. A. 1974, A&AS, 15, 417
Holdship, J., Viti, S., Jimenez-Serra, I., et al. 2016, MNRAS, 463, 802
Howk, J. C., Sembach, K. R., & Savage, B. D. 2006, ApJ, 637, 333
Huang, J., Andrews, S. M., Cleeves, L. I., et al. 2018, ApJ, 852, 122
Huang, J., Andrews, S. M., Dullemond, C. P., et al. 2020, ApJ, 891, 48
Huang, J., Bergin, E. A., Öberg, K. I., et al. 2021, ApJS, 257, 19
Huang, J., Öberg, K. I., & Andrews, S. M. 2016, ApJL, 823, L18
Huang, J., Öberg, K. I., Qi, C., et al. 2017, ApJ, 835, 231
Hunter, J. D. 2007, CSE, 9, 90
Ilee, J. D., Walsh, C., Booth, A. S., et al. 2021, ApJS, 257, 9
Ingleby, L., Espaillat, C., Calvet, N., et al. 2015, ApJ, 805, 149
Jenkins, E. B. 2009, ApJ, 700, 1299
Jones, A. P., & Ysard, N. 2019, A&A, 627, A38
Jones, E., Oliphant, T., Peterson, P., et al. 2001, SciPy: Open Source Scientific Tools for Python, http://www.scipy.org/
Kama, M., Shorttle, O., Jermyn, A. S., et al. 2019, ApJ, 885, 114
Kastner, J. H., Qi, C., Dickson-Vandervelde, D. A., et al. 2018, ApJ, 863, 106
Keller, L. P., Hony, S., Bradley, J. P., et al. 2002, Natur, 417, 148
Klaassen, P. D., Juhasz, A., Mathews, G. S., et al. 2013, A&A, 555, A73
Kolesniková, L., Tercero, B., Cernicharo, J., et al. 2014, ApJL, 784, L7
Kraus, A. L., & Hillenbrand, L. A. 2009, ApJ, 704, 531
Kurucz, R. L. 1993, SYNTHE Spectrum Synthesis Programs and Line Data (Cambridge, MA: Smithsonian Astrophysical Observatory)
Laas, J. C., & Caselli, P. 2019, A&A, 624, A108
Law, C., Loomis, R. A., & Teague, R. 2021, ApJS, 257, 3
Le Gal, R., Brady, M. T., Öberg, K. I., Roueff, E., & Le Petit, F. 2019a, ApJ, 886, 86
Le Gal, R., Herbst, E., Dufour, G., et al. 2017, A&A, 605, A88
Le Gal, R., Öberg, K. I., Loomis, R. A., Pegues, J., & Bergner, J. B. 2019b, ApJ, 876, 72
Lellouch, E., McGrath, M. A., & Jessup, K. L. 2007, in Io After Galileo: A New View of Jupiter's Volcanic Moon, ed. R. M. C. Lopes & J. R. Spencer (Berlin: Springer), 231
Liu, Y., Dipierro, G., Ragusa, E., et al. 2019, A&A, 622, A75
Loomis, R. A., Cleeves, L. I., Öberg, K. I., et al. 2018a, ApJ, 859, 131
Loomis, R. A., Öberg, K. I., Andrews, S. M., et al. 2018b, AJ, 155, 182
Loomis, R. A., Öberg, K. I., Andrews, S. M., et al. 2020, ApJ, 893, 101
Macías, E., Espaillat, C. C., Ribas, Á, et al. 2018, ApJ, 865, 37
Mawet, D., Absil, O., Montagnier, G., et al. 2012, A&A, 544, A131
McMullin, J. P., Waters, B., Schiebel, D., Young, W., & Golap, K. 2007, in ASP Conf. Ser., 376, Astronomical Data Analysis Software and Systems XVI, ed. R. A. Shaw, F. Hill, & D. J. Bell (San Francisco, CA: ASP), 127
Meier, R., & A'Hearn, M. F. 1997, Icar, 125, 164
Mendigutía, I., Brittain, S., Eiroa, C., et al. 2013, ApJ, 776, 44
Millar, T. J., & Herbst, E. 1990, A&A, 231, 466
Montesinos, B., Eiroa, C., Mora, A., & Merín, B. 2009, A&A, 495, 901
Müller, H. S. P., Schlöder, F., Stutzki, J., & Winnewisser, G. 2005, JMoSt, 742, 215
Müller, H. S. P., Thorwirth, S., Roth, D. A., & Winnewisser, G. 2001, A&A, 370, L49
Navarro-Almaida, D., Le Gal, R., Fuente, A., et al. 2020, A&A, 637, A39
Neufeld, D. A., Godard, B., Gerin, M., et al. 2015, A&A, 577, A49
Nilsson, A., Hjalmarson, Å., Bergman, P., & Millar, T. J. 2000, A&A, 358, 257
Öberg, K. I., & Bergin, E. A. 2021, PhR, 893, 1
Öberg, K. I., Guzmán, V. V., & Walsh, C. 2021, ApJS, 257, 1
Öberg, K. I., Qi, C., Fogel, J. K. J., et al. 2011, ApJ, 734, 98
Pacheco-Vázquez, S., Fuente, A., Baruteau, C., et al. 2016, A&A, 589, A60
Palumbo, M. E., Geballe, T. R., & Tielens, A. G. G. M. 1997, ApJ, 479, 839
Palumbo, M. E., Tielens, A. G. G. M., & Tokunaga, A. T. 1995, ApJ, 449, 674
Phuong, N. T., Chapillon, E., Majumdar, L., et al. 2018, A&A, 616, L5
Piétu, V., Dutrey, A., & Guilloteau, S. 2007, A&A, 467, 163
Pinte, C., Ménard, F., Duchêne, G., et al. 2018, A&A, 609, A47
Podio, L., Lefloch, B., Ceccarelli, C., Codella, C., & Bachiller, R. 2014, A&A, 565, A64
Pontoppidan, K. M., Salyk, C., Banzatti, A., et al. 2019, ApJ, 874, 92
Ranjan, S., Todd, Z. R., Sutherland, J. D., & Sasselov, D. D. 2018, AsBio, 18, 1023
Rivière-Marichalar, P., Fuente, A., Goicoechea, J. R., et al. 2019, A&A, 628, A16
Rivière-Marichalar, P., Fuente, A., Le Gal, R., et al. 2020, A&A, 642, A32
Ruf, A., Bouquet, A., Boduch, P., et al. 2019, ApJL, 885, L40
Ruffle, D. P., Hartquist, T. W., Caselli, P., & Williams, D. A. 1999, MNRAS, 306, 691
Salyk, C., Herczeg, G. J., Brown, J. M., et al. 2013, ApJ, 769, 21
Semenov, D., Favre, C., Fedele, D., et al. 2018, A&A, 617, A28
Shakura, N. I., & Sunyaev, R. A. 1973, A&A, 24, 337
Shirley, Y. L. 2015, PASP, 127, 299
Sierra, A., Pérez, L. M., Zhang, K., et al. 2021, ApJS, 257, 14
Simon, M., Guilloteau, S., Beck, T. L., et al. 2019, ApJ, 884, 42
Teague, R. 2019, JOSS, 4, 1632
Teague, R., Bae, J., & Bergin, E. A. 2019, Natur, 574, 378
Teague, R., Bae, J., Birnstiel, T., & Bergin, E. A. 2018a, ApJ, 868, 113
Teague, R., & Foreman-Mackey, D. 2018, RNAAS, 2, 173
Teague, R., Henning, T., Guilloteau, S., et al. 2018b, ApJ, 864, 133
Teague, R., Bae, J., Aikawa, Y., et al. 2021, ApJS, 257, 18
Tieftrunk, A., Pineau des Forets, G., Schilke, P., & Walmsley, C. M. 1994, A&A, 289, 579
van der Plas, G., Casassus, S., Ménard, F., et al. 2014, ApJL, 792, L25
van der Tak, F. F. S., Lique, F., Faure, A., Black, J. H., & van Dishoeck, E. F. 2020, Atoms, 8, 15
van der Walt, S., Colbert, S. C., & Varoquaux, G. 2011, CSE, 13, 22
van der Walt, S., Schönberger, J. L., Nunez-Iglesias, J., et al. 2014, arXiv:1407.6245
van Dishoeck, E. F., & Blake, G. A. 1998, ARA&A, 36, 317
van Dishoeck, E. F., Kristensen, L. E., Mottram, J. C., et al. 2021, A&A, 648, A24
Vastel, C., Quénard, D., Le Gal, R., et al. 2018, MNRAS, 478, 5514
Vidal, T. H. G., Loison, J.-C., Jaziri, A. Y., et al. 2017, MNRAS, 469, 435
Wagenblast, R., & Hartquist, T. W. 1989, MNRAS, 237, 1019
Wakelam, V., Caselli, P., Ceccarelli, C., Herbst, E., & Castets, A. 2004, A&A, 422, 159
Wakelam, V., Chapillon, E., Dutrey, A., et al. 2019, MNRAS, 484, 1563
Wakelam, V., & Herbst, E. 2008, ApJ, 680, 371
Wakelam, V., Loison, J. C., Mereau, R., & Ruaud, M. 2017, MolAs, 6, 22
Wakelam, V., Ruaud, M., Hersant, F., et al. 2016, A&A, 594, A35
Whittet, D. C. B. 2010, ApJ, 710, 1009
Wiesenfeld, L., & Faure, A. 2013, MNRAS, 432, 2573
Yen, H.-W., Koch, P. M., Liu, H. B., et al. 2016, ApJ, 832, 204